HAL open science

A sub-Neptune planet around TOI-1695 discovered and characterized with SPIRou and TESS

Flavien Kiefer, Guillaume H. Hébrard, Eder Martioli, Étienne Artigau, René Doyon, Jean François Donati, Charles Cadieux, Andres Carmona, David R. Ciardi, P. I. Cristofari, et al.

To cite this version:

Flavien Kiefer, Guillaume H. Hébrard, Eder Martioli, Étienne Artigau, René Doyon, et al.. A sub-Neptune planet around TOI-1695 discovered and characterized with SPIRou and TESS. Astronomy and Astrophysics - A&A, 2023, 670, A136 (28p.). 10.1051/0004-6361/202245129 . hal-04069281

HAL Id: hal-04069281

https://hal.science/hal-04069281v1

Submitted on 6 Jun 2023

HAL is a multi-disciplinary open access archive for the deposit and dissemination of scientific research documents, whether they are published or not. The documents may come from teaching and research institutions in France or abroad, or from public or private research centers.

L'archive ouverte pluridisciplinaire **HAL**, est destinée au dépôt et à la diffusion de documents scientifiques de niveau recherche, publiés ou non, émanant des établissements d'enseignement et de recherche français ou étrangers, des laboratoires publics ou privés.

Distributed under a Creative Commons Attribution 4.0 International License

A&A 670, A136 (2023)
https://doi.org/10.1051/0004-6361/202245129
© The Authors 2023

Astronomy & Astrophysics

A sub-Neptune planet around TOI-1695 discovered and characterized with SPIRou and TESS

F. Kiefer[1,2], G. Hébrard[2,3], E. Martioli[4,2], E. Artigau[5], R. Doyon[5], J.-F. Donati[6], C. Cadieux[5], A. Carmona[7], D. R. Ciardi[8], P. I. Cristofari[6], L. de Almeida[4], P. Figueira[11,12], E. Gaidos[28], E. Gonzales[9], A. Lecavelier Des Etangs[2], K. G. Stassun[10], L. Arnold[13], B. Benneke[14], I. Boisse[15], X. Bonfils[7], N. J. Cook[5], P. Cortés-Zuleta[15], X. Delfosse[7], J. Dias do Nascimento[33,34], M. Fausnaugh[16], W. Fong[16], P. Fouqué[5], T. Forveille[7], J. Gomes da Silva[25], K. Hesse[16], Á. Kóspál[29,30,31,32], H. Lewis[17], C.-F. Liu[27], J. H. C. Martins[25], M. Paegert[18], S. Seager[19,20,21], H. Shang[27], J. D. Twicken[22,23], T. Vandal[5], S. Vinatier[1], T. Widemann[1,26], and J. N. Winn[24]

(Affiliations can be found after the references)

Received 3 October 2022 / Accepted 8 November 2022

ABSTRACT

TOI-1695 is a V-mag = 13 M-dwarf star from the northern hemisphere at 45 pc from the Sun, around which a 3.134-day periodic transit signal from a super-Earth candidate was identified in TESS photometry. With a transit depth of 1.3 mmag, the radius of candidate TOI-1695.01 was estimated by the TESS pipeline to be 1.82 $R_\oplus$ with an equilibrium temperature of ~620 K. We successfully detected a reflex motion of the star and establish that it is due to a planetary companion at an orbital period consistent with the photometric transit period, thanks to a year-long radial-velocity monitoring of TOI-1695 by the SPIRou infrared spectropolarimeter. We used and compared different methods to reduce and analyze those data. We report a 5.5σ detection of the planetary signal, giving a mass of 5.5±1.0 $M_\oplus$ and a radius of 2.03±0.18 $R_\oplus$. We derive a mean equilibrium planet temperature of 590±90 K. The mean density of this small planet of 3.6±1.1 g cm^{-3} is similar (1.7σ lower) than that of the Earth. It leads to a nonnegligible fraction of volatiles in its atmosphere with $f_{\rm H,He} = 0.28^{+0.46}_{-0.23}$% or $f_{\rm water}$ = 23±12%. TOI-1695 b is a new sub-Neptune planet at the border of the M-dwarf radius valley that can help test formation scenarios for super-Earth and sub-Neptune-like planets.

Key words. planets and satellites: detection – planets and satellites: fundamental parameters – planets and satellites: individual: TOI-1695 b – techniques: photometric – techniques: radial velocities

1. Introduction

Over the next few years, new space- and ground-based observatories (e.g., the *James Webb* Space Telescope – JWST and the ESO Extremely Large Telescope – ELT) will be crucial to extending the current boundaries of planetary science. These instruments will boost the exploration of the atmospheres of exoplanets to an unprecedented level of precision, and probe the gas content of super-Earths and terrestrial exoplanets. It is thus of key importance to identify new low-mass exoplanets amenable to future atmospheric characterization.

A central feature of small exoplanets ($R < 4\,R_\oplus$) at small orbital separation ($P < 100$ days) is the radius valley (Owen & Wu 2013; Fulton et al. 2017; Cloutier & Menou 2020) separating solid super-Earths from gaseous sub-Neptunes. One possible explanation for this dichotomy is runaway evaporation or grinding of the atmospheres of low-mass exoplanets by a strong extreme ultraviolet (XUV) stellar radiation (Owen & Wu 2013). Alternative explanations are core-powered mass loss (Ginzburg et al. 2018), impact erosion by planetesimals (Shuvalov 2009), and formation of distinct rocky and non-rocky planet populations with delayed gas accretion (Lee et al. 2014; Lee & Connors 2021). Around solar-like stars, photoevaporation and core-powered mass loss scenarios predict that the valley location shifts toward a lower radius with lower stellar mass and larger orbital period (Van Eylen et al. 2018; Fulton & Petigura 2018; Martinez et al. 2019; Wu 2019; Gupta et al. 2022).

Around low-mass stars, Cloutier & Menou (2020) find that the slope of the valley around M-dwarfs in the radius-period diagram is inverse to the valley slope around FGK stars, leading to increasing radius of the transition with orbital period. This relationship is more compatible with a gas-depleted planet formation scenario in which solid cores increase in size with increasing distance to the star (Lee et al. 2014; Lopez & Rice 2018). Similarly to solar-like stars, for planets around low-mass stars, photoevaporation and core-powered mass loss are also expected to shape a radius gap with a negative slope in $R_p - P$ diagram. However, this slope is expected to approach closer and closer to zero with decreasing stellar mass (Gupta et al. 2022).

Here we characterize a candidate planet with super-Earth-to-sub-Neptune size, that was detected and identified around the M2-type star TOI-1695, with the NASA Transiting Exoplanet Survey Satellite (TESS; Ricker et al. 2015). With an initially estimated radius of 1.8 $R_\oplus$ and an orbital period of 3.134 days, TOI-1695.01 lies in a radius–separation region where the question of formation and evolution of the atmosphere of super-Earth or sub-Neptune around a low-mass star can be tackled. Investigating whether or not such a key planet harbors a significant atmosphere may help explain which scenario is dominantly shaping the radius valley depending on the host star mass.

Open Access article, published by EDP Sciences, under the terms of the Creative Commons Attribution License (https://creativecommons.org/licenses/by/4.0), which permits unrestricted use, distribution, and reproduction in any medium, provided the original work is properly cited.
This article is published in open access under the Subscribe to Open model. Subscribe to A&A to support open access publication.

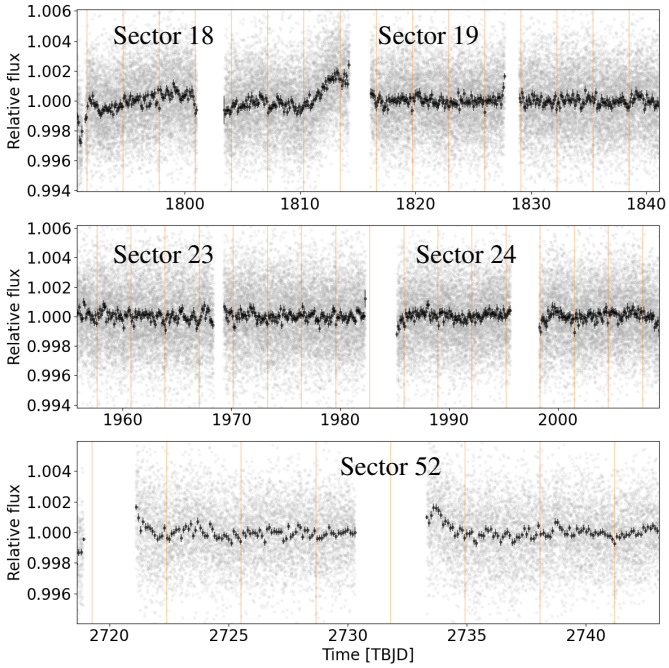

Fig. 1. Full TESS light curve separated in sectors (gray dots) and binned with a 0.1-day timestep (black). The identified transit locations are shown as orange vertical lines.

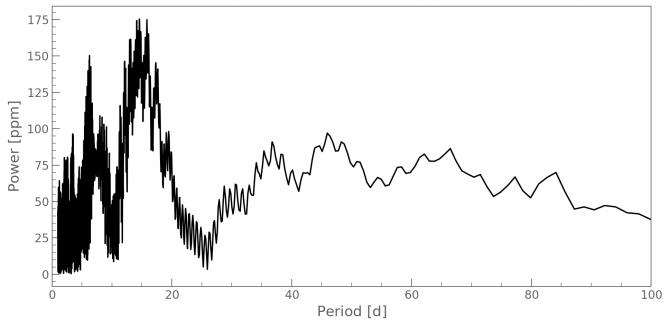

Fig. 2. Periodogram of the TESS SPOC light curve with a peak at ~15 days for a 175 ppm signal.

In this paper we seek to first establish the planetary nature of TOI-1695.01, and to characterize its mass and radius by combining TESS photometric measurements with radial velocity (RV) variations observed with the infrared (0.98–2.45 µm) SpectroPolarimetre InfraRouge (SPIRou; Donati et al. 2020) installed on the 3.6m Canada-France-Hawaii Telescope (CFHT).

In Sect. 2 we review the observations available for TOI-1695, including those from TESS and SPIRou. In Sect. 3 we characterize the host star using spectroscopy, spectrophotometry, and spectropolarimetry. In Sect. 4 we characterize the planet properties through a joint fit of TESS and SPIRou data. In Sect. 5 we discuss the results. We summarize and conclude in Sect. 6.

2. Observations

2.1. TESS light curves

TOI-1695, also known as TIC-422756130.01 in the TESS Input Catalog (TIC), was covered by TESS sectors 18, 19, 24, 25, and 52 between November 2019 and June 2022 with 120 s cadence. In the data from these observing campaigns, a signal at a 3.13-day period is found using the box least squares (BLS) algorithm (Kovács et al. 2002) with 34 transits found, of which 32 were already identified in the data validation time series (hereafter DVT; Twicken et al. 2018; Li et al. 2019) of sectors 18–25, allowing the event TOI-1695.01 to be identified. We retrieved and used in the rest of this study the Science Processing Operations Center Pipeline (SPOC; Jenkins et al. 2016) simple aperture photometry with presearch data conditioning (PDCSAP ; Smith et al. 2012; Stumpe et al. 2014). The full SPOC PDCSAP light curve with all identified transits is shown in Fig. 1.

We first performed a preliminary fit of the TESS PDCSAP data of TOI-1695 by a photometric `batman` model (Kreidberg 2015) with a third-degree polynomial modeling of the continuum of all individual transits. It has a transit depth of ~1000 ppm for a total transit duration of 1.2 h and a period of 3.134319±0.000026 days. It was pointed out[1] that the SPOC photometry pipeline was prone to overestimating the background level and overcorrecting for background in crowded fields in the TESS primary mission (sectors 1–26). The pipeline was updated to prevent this in the extended mission (sectors 27+). We estimate that the combined transit search of the TOI 1695 data for sectors 18, 19, 24, 25, and 52 would have overestimated the transit depth (planet radius) by approximately 2.8% (1.4%). This is a minor correction compared to the uncertainties (~8.9%) resulting from the full analysis performed in Sect. 4.

Using `TRICERATOPS` (Giacalone & Dressing 2020), we examined possible sources of false-positive (FP) transit detection in the TOI-1695 light curve, from the system itself and from nearby background systems within the TESS aperture. The full list of possible causes of a FP is given in Table 1 of Giacalone et al. (2021). We show the aperture used in sector 18 and possible contaminating sources around TOI-1695 in Fig. A.1. This source is located in a crowded region with 411 neighbors with T-mag<18 at less than 200″. At most eight stars identified in the different TESS apertures could be contributing to the transit signal with TIC IDs 422756137, 422756132, 422756120, 629325853, 422756126, 422756145, 422756114, and 422756147. They have a flux ratio with TOI-1695 in the TESS passband between 5.3 and 7.4 mag. We find an FP probability of transit from TOI-1695 itself of 0.18% and an FP probability of background star pollution of 0.10%. These probabilities account for the contrast curve around TOI-1695 obtained in Sect. 2.3. According to the criteria defined by Giacalone et al. (2021), TOI-1695 b is thus a "validated" planet. Nevertheless, complementary follow-up with RV, as performed in the present paper, is necessary to independently validate its planetary nature and measure its mass.

Beyond the transit signal, a 15-day modulation with an average amplitude of ~175 ppm seems to be present in the PDCSAP light curves. A periodogram of the TESS PDCSAP data produced with `lightkurve` (Lightkurve Collaboration 2018) is shown in Fig. 2. This 15-day periodic signal is in fact mainly seen in Sector 18 with an amplitude of ~700 ppm (Fig. 1). We discard effects from variable background stars since, given the sources identified above within TOI-1695 apertures, such amplitude of variations in the light curve would require those sources to have proper oscillations >10%, which is rare (McQuillan et al. 2012). If not of instrumental origin, which we cannot fully exclude, this fluctuating signal could well be due to spots, in which case the 15-day period would be linked with the rotation period of the

[1] https://archive.stsci.edu/missions/tess/doc/tess_drn/tess_sector_27_drn38_v02.pdf

star. We discuss this possibility in more detail and compare it to other observations in Sect. 3.4.

2.2. SPIRou spectra

2.2.1. Observations

SPIRou is a near-infrared high-resolution (980–2450 nm; $R = 75{,}000$) high-stability ($\sim$1 m s^{-1}) velocimeter and spectropolarimeter installed at the Cassegrain focus of the 3.6 m CFHT at Mauna Kea (Donati et al. 2020). TOI-1695 was observed between December 2020 and January 2022 with SPIRou as part of the large program SPIRou Legacy Survey (SLS; ID P42, PI: Jean-François Donati). It was observed at 45 observing epochs with four polarimetric exposures per epoch, totaling 180 SPIRou spectra. Table F.1 presents the observation log associated with each exposure. All SPIRou observations of TOI-1695 consist of polarization sequences, each split into four sub-exposures associated with different rhomb retarder configurations, from which we retrieve the corresponding Stokes I (unpolarized) and V (circularly polarized) spectra of the star at each epoch (Donati et al. 2020). The sequence number 1–4 of any sub-exposure is also given in Table F.1. Science data are acquired on fibers A and B fed by the two orthogonal states of the selected polarization, while fiber C is used to simultaneously record the spectrum of the SPIRou Fabry-Pérot RV reference, as described in Hobson et al. (2021).

A calibration sequence, including flats, darks, and spectra of comparison lamps (Fabry-Pérot, UNe), is performed every afternoon and morning, preceding and following each night of observation with SPIRou. A master-dark is constructed from a subset of well-characterized darks. The SPIRou detector software also archives ramp-files, which are detector images in ADU/s; during their creation a correction for nonlinearity is performed. Early-type stars (A-type) are observed nightly as telluric absorption standards. Bright inactive cool stars are also regularly observed as RV standards. These data are used to calibrate the measurements extracted from the SPIRou spectra. The detailed calibration sequence is described in Cook et al. (2022).

2.2.2. APERO reduction

The raw data were first reduced with the SPIRou reduction software, A PipelinE to Reduce Observations (APERO) with version 0.6.132 (Cook et al. 2022), hereafter v6. APERO first corrects detector effects, removes constant background thermal components, and identifies bad pixels and cosmic-ray impacts. It then calculates the position of 49 of the 50 echelle spectral orders[2] and optimally extracts spectra from fibers A, B, and C into 2D order-separated e2ds and 1D order-merged s1d spectra. A blaze function is derived from the flat-field exposures.

The wavelengths are calibrated on the spectrum collected on Fiber C. An absolute calibration of wavelengths with respect to the Solar System barycentric rest frame using the current Barycentric Earth RV (BERV) and the Barycentric Julian Date (BJD) of each exposure is performed by the code `barycorrpy` (Kanodia & Wright 2018; Wright & Eastman 2014). Finally, for each exposure (`e.fits` file) APERO calculates the corresponding spectrum of the telluric transmission out of the whole collection of standard star observations carried out with SPIRou since 2018 using PCA algorithm (Artigau et al. 2014) and divides it out, producing a telluric-corrected `t.fits` spectrum. APERO also calculates the Stokes V spectra using the method of Donati et al. (1997), as described in detail in Martioli et al. (2020).

A more advanced version of the APERO pipeline, version 0.7.194, hereafter v7, was released during the writing of this work (Artigau et al. 2022; Cadieux et al. 2022). We used both v6 and v7 in our study, and compare them in Sect. 4.

2.2.3. RV derivation

The RV were derived from the telluric corrected `t.fits` spectra using the line-by-line (LBL) algorithm (Artigau et al. 2022). As in Bouchy et al. (2001), LBL requires a template spectrum with a S/N that is as high as possible since a derivative of the template is used to determine the RV of each spectral line. For TOI-1695, with only 40 epochs, the combined spectrum produced by APERO reaches a S/N that is much lower than other bright standard stars monitored with SPIRou. Instead of TOI-1695, we thus used as template another target with a similar M2V spectral type, GL15A ($T_{\rm eff} = 3600$ K; $\log g = 4.8$ cgs units; [M/H] = -0.16 dex; Passegger et al. 2019; Cristofari et al. 2022b). Table 2 shows the stellar parameters that we find for TOI-1695. We combined 1040 spectra of GL15A with for each a $S/N \sim 350$ at 1670 nm leading to a template with S/N close to 10 000.

The second and third derivatives of each spectral line are used as a proxy for the full width at half maximum (FWHM) and bisector span (BIS; Artigau et al. 2022). Their variations with respect to RV are studied in Sect. 3.3.

Calibration drifts are derived for all RV measurement epochs using the simultaneous Fabry-Pérot on fiber C. They lead to drift-corrected (DC) RVs. An average zero-point correction (ZPC) is also derived from the monitoring of RV standards (Cadieux et al. 2022). Our reference RVs in the rest of the paper will be those corrected from drift and zero-point, but we do a comparison of RV data reduction with or without DC and ZPC when analyzing the planet signal in Sect. 4.

All RV data, FWHM and BIS used for TOI-1695 and reduced with versions v6 and v7 are available in Tables G.1 and G.2, respectively. Their variations are inspected in greater detail in Sect. 3.3. In both cases we ignored the measurement of epoch 44 (JD−2459605), which only has a single sub-exposure. With v6, we also ignored the measurements of epoch 33 (JD−2459591), for which the drift calculation failed.

2.3. Imaging

As part of a standard process to validate transiting exoplanets and to assess the possible contamination of bound or unbound companions on the derived planetary radii (Ciardi et al. 2015), TOI-1695 was observed with infrared high-resolution adaptive optics (AO) imaging at Keck Observatory with the NIRC2 instrument on Keck-II behind the natural guide star AO system (Wizinowich et al. 2000). The observations were made on 2020 May 28 UT in the standard three-point dither pattern that is used with NIRC2 to avoid the lower left quadrant of the detector, which is typically noisier than the other three quadrants. The dither pattern step size was 3″ and was repeated twice, with each dither offset from the previous dither by 0.5″. The camera was in the narrow-angle mode with a full field of view of $\sim$10″ and a pixel scale of approximately 0.01″ per pixel. The observations were made in the narrowband Br-γ filter ($\lambda_o = 2.17$ µm; $\Delta\lambda = 0.03$ µm) with an integration time of 4 s with one coadd per frame for a total of 36 s on target.

The AO data were processed and analyzed with a custom set of IDL tools. The science frames were flat-fielded and

[2] APERO does not extract the bluest order due to low S/N.

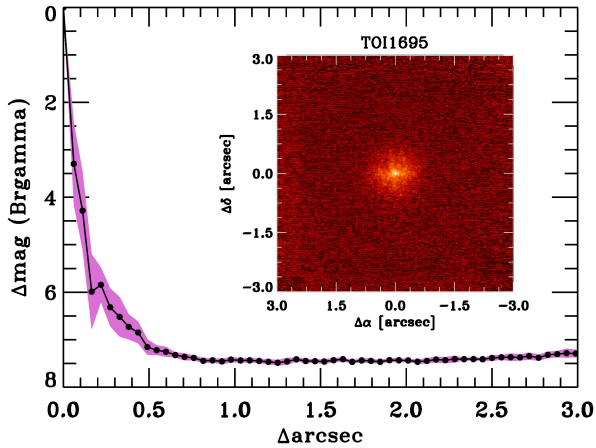

Fig. 3. Companion sensitivity for the Keck NIR adaptive optics imaging. The black points represent the 5σ limits and are separated in steps of 1 FWHM (~0.054″); purple represents the azimuthal dispersion (1σ) of the contrast determinations (see text). The inset image is of the primary target showing no additional companions to within 3″ of the target.

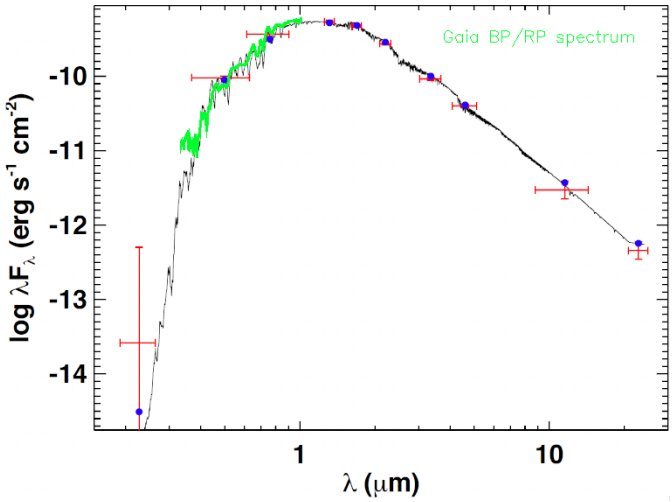

Fig. 4. Spectral energy distribution of TOI-1695. Red symbols represent the observed photometric measurements, where the horizontal bars represent the effective width of the passband. Blue symbols are the model fluxes from the best-fit NextGen atmosphere model (black curve). The green curve is the published *Gaia* DR3 spectrum for this star.

sky-subtracted. The flat fields were generated from a median of dark subtracted flats taken on-sky, and the flats were normalized such that the median value of the flats is unity. Sky frames were generated from the median average of the nine dithered science frames; each science image was then sky-subtracted and flat-fielded. The reduced science frames were combined into a single combined image using an intra-pixel interpolation that conserves flux, shifts the individual dithered frames by the appropriate fractional pixels, and median-coadds the frames. The final resolution of the combined dithers was determined from the FWHM of the point spread function to 0.054″.

The sensitivities of the final combined AO image were determined by injecting simulated sources azimuthally around the primary target every 20° at separations of integer multiples of the central source's FWHM (Furlan et al. 2017). The brightness of each injected source was scaled until standard aperture photometry detected it with 5σ significance. The resulting brightness of the injected sources relative to the target set the contrast limits at that injection location. The final 5σ limit at each separation was determined from the average of all of the determined limits at that separation and the uncertainty on the limit was set by the RMS dispersion of the azimuthal slices at a given radial distance.

No additional companions to within the limits of the data were detected (see Fig. 3). With contrast sensitivities of ~3.5 mag at 0.06″ (2.7 au) and ~7 mag at 0.5″ (22 au), the near-infrared (NIR) AO observations indicate that there are likely no stellar companions down to ~M6 - L9 (see E. Mamajek's compilation of Mean Dwarf Stellar Colors version 2021.03.02[3]).

3. Stellar characterization

3.1. Stellar parameters

We used four different methods to measure the stellar parameters of the star, including the effective temperature $T_{\rm eff}$, the surface gravity $\log g$, the metallicity [M/H], the micro-turbulent $v_{\rm micro}$, the macro-turbulent velocity $v_{\rm macro}$, the bolometric flux $F_{\rm bol}$, the bolometric luminosity $\mathcal{L}_{\rm bol}$, the stellar mass $M_\star$, and the stellar radius $R_\star$. The methods of spectral energy distribution (SED) and of the TESS Exoplanet Follow-up Observing Program (exoFOP[4] are summarized in Sect. 3.1.1). The methods of comparison to synthetic spectra, based on SPIRou spectra, are explained in Sect. 3.1.2. All results are summarized and compared in Table 2.

3.1.1. Spectral energy distribution

We performed an analysis of the broadband SED of the star together with the *Gaia* EDR3 parallax (with no systematic offset applied; see in particular Stassun & Torres 2021), in order to determine an empirical measurement of the stellar radius, following the procedures described in Stassun & Torres (2016) and Stassun et al. (2017, 2018). We retrieved the JHK_S magnitudes from 2MASS, the W1–W4 magnitudes from WISE, and the $G_{\rm BP}G_{\rm RP}$ magnitudes from *Gaia*, as well as the near-ultraviolet (NUV) flux from GALEX. Together, the available photometry spans the stellar SED over the wavelength range 0.2–22 μm (see Fig. 4). All photometric data are summarized in Table 1.

We performed a fit using NextGen stellar atmosphere models (Hauschildt et al. 1999), with the free parameters being effective temperature ($T_{\rm eff}$) and metallicity ([Fe/H]), as well as extinction A_V, which we limited to maximum line-of-sight value from the Galactic dust maps of Schlegel et al. (1998). The resulting fit (Fig. 4) has a best-fit $A_V = 0.02 \pm 0.02$, $T_{\rm eff} = 3630 \pm 50$ K, and [Fe/H] = 0.0 ± 0.5, with a reduced χ^2 of 1.3. It also fits well with the calibrated mean *Gaia* BP/RP magnitudes spectrum available for this star in *Gaia* DR3 (Montegriffo et al. 2023) as shown in Fig. 4. Integrating the (unreddened) model SED gives the bolometric flux at Earth, $F_{\rm bol} = 6.82 \pm 0.24 \times 10^{-10}$ erg s^{-1} cm^{-2}, which with the *Gaia* parallax gives directly the bolometric luminosity, $L_{\rm bol} = 0.0431 \pm 0.0015\ L_\odot$. Taking the $F_{\rm bol}$ and $T_{\rm eff}$ together with the *Gaia* parallax gives the stellar radius, $R_\star = 0.525 \pm 0.017\ R_\odot$. In addition, we can estimate the stellar mass from the empirical M_K relations of

[3] https://www.pas.rochester.edu/~emamajek/EEM_dwarf_UBVIJHK_colors_Teff.txt

[4] https://exofop.ipac.caltech.edu/tess/

Table 1. Main astrometric and photometric data of TOI-1695.

Parameter	Unit	Value	Ref.
TIC		422756130	
Gaia DR2/EDR3		534988616816537728	
2MASS		J01274094+7217472	
WISE		J012741.12+721747.6	
RA	ICRS (J2000)	01:27:40.973	1
DEC	ICRS (J2000)	+72:17:47.186	1
PM RA μ_α	mas yr^{-1}	71.628±0.013	1
PM Dec μ_δ	mas yr^{-1}	40.450±0.019	1
Epoch		2016.0	1
Gaia DR3 parallax	(mas)	22.226±0.014	1
distance	(pc)	45.131±0.068	1
Gaia $G_{\rm BP}$	mag	13.3064±0.0040	1
Gaia G	mag	12.1275±0.0011	1
Gaia $G_{\rm RP}$	mag	11.0464±0.0022	1
TESS T	mag	11.0294±0.0074	
2MASS J	mag	9.640±0.024	2
2MASS H	mag	8.984±0.028	2
2MASS K	mag	8.818±0.021	2
WISE 3.4 µm	mag	8.684±0.024	3
WISE 4.6 µm	mag	8.61±0.02	3
WISE 12 µm	mag	8.511±0.027	3
WISE 22 µm	mag	8.40±0.29	3

References. (1) Gaia Collaboration (2021); (2) Cutri et al. (2003); (3) Wright et al. (2010).

Mann et al. (2019), giving $M_\star = 0.539 \pm 0.027\ M_\odot$. These mass and radius values lead to $\log g = 4.72 \pm 0.14$ in cgs units.

The stellar parameters from the TESS project can be found in the TESS-exoFOP and are also reported in Table 2. TOI-1695 belongs to the specially curated list of cool dwarfs of the TIC (Muirhead et al. 2018; Stassun et al. 2019). As explained in Stassun et al. (2019), the effective temperature $T_{\rm eff}$ is retrieved from the cool dwarfs catalog of TIC v7 (Stassun et al. 2018). The radius is derived from the $T_{\rm eff}$, *Gaia* magnitudes, and *Gaia* parallax using Eq. (4) of Stassun et al. (2019). The mass is obtained from the spline-interpolation of an empirical mass-$T_{\rm eff}$ relationship.

The parameters derived from the two methods are consistent within the uncertainties.

3.1.2. Comparison to synthetic spectra

We also derive the stellar parameters for TOI-1695 from a high-resolution template spectrum built from the tens of individual spectra acquired with SPIRou. The method used consists in the comparison of a grid of synthetic spectra to the template spectrum. We use two independent methods, both based on MARCS models (Gustafsson et al. 2008).

The first method is based on a process briefly described below (more details in Cristofari et al. 2022b,a). This process was tested and calibrated on reference stars. The synthetic spectra used for this analysis were computed from the MARCS model atmospheres with the `Turbospectrum` radiative transfer code (Plez 2012), for a wide range of effective temperatures ($T_{\rm eff}$), surface gravities ($\log g$), and metallicities ([M/H]). The models and template spectrum are compared by computing a χ^2 value in key regions, containing lines that are both well reproduced by the models and sensitive to the stellar parameters. We therefore retrieve a three-dimensional grid of χ^2 values, and perform a paraboloid fit to identify the best-fitting parameters and estimate error bars on these values. For TOI-1695, the parameters estimated with this method are $T_{\rm eff} = 3627 \pm 31$ K, $\log g = 4.60 \pm 0.05$ dex, and [M/H] = 0.10 ± 0.10 dex. A fit of the star's projected rotational velocity $v \sin i$, fixing the micro-turbulent velocity to $v_{\rm micro} = 1\,{\rm km\,s^{-1}}$, the macro-turbulence velocity to $v_{\rm macro} = 0\,{\rm km\,s^{-1}}$, and the resolution linewidth of SPIRou to $FWHM \sim 4.3\,{\rm km\,s^{-1}}$, leads to a $v \sin i = 1.9 \pm 0.2\,{\rm km\,s^{-1}}$. Given that $v_{\rm macro}$ is fixed to 0, we can only interpret this measurement as an upper limit on $v \sin i$; therefore, $<2.5\,{\rm km\,s^{-1}}$ at 1σ, which is at most on the order of the pixel scale of the SPIRou detector ($\sim 2.3\,{\rm km\,s^{-1}}$; Donati et al. 2020). Modeled and observed spectral lines are compared together in Fig. B.1.

The second method used is described in greater detail in Sect. 4.2 in Martioli et al. (2022). We calculated a grid of 650 000 synthetic spectra generated with `MOOG` (Sneden et al. 2012) covering $T_{\rm eff}$ from 2900 to 4100 K with 50 K step, $\log g$ from 3.5 to 5.3 with 0.1 dex step, [M/H] from −0.6 to 0.5 with 0.11 dex step, alpha from −0.2 to 0.4 with 0.06 dex step, and $v_{\rm mic}$ from 0.5 to $4\,{\rm km\,s^{-1}}$ with $0.35\,{\rm km\,s^{-1}}$ step. We modified the Apache Point Observatory Galactic Evolution Experiment (APOGEE) line list (Smith et al. 2021) by selecting only the lines that are most sensitive to $T_{\rm eff}$ and $\log g$ within the spectral range from 1.5 to 1.7 µm. We searched the grid for the best-fitting parameters, which are adopted as priors in the `iSpec` integrator (Blanco-Cuaresma 2019) to calculate the synthetic spectrum that best fits our SPIRou data within the domain of the selected lines. We used the `MOOG` code with the MARCS GES model (Gustafsson et al. 2008) and Asplund et al. (2009) solar abundances. In total, 78 spectra were compared. The parameters of TOI-1695 estimated with this method are $T_{\rm eff} = 3711 \pm 47$ K, $\log g = 4.53 \pm 0.13$ dex, [M/H] = 0.00 ± 0.08 dex, and $v_{\rm micro} = 0.3 \pm 0.7\,{\rm km\,s^{-1}}$.

The values derived with these two methods agree well with each other; moreover, there is good agreement with the SED fitting at 2σ. In the rest of the analysis we thus adopt the values $T_{\rm eff} = 3650 \pm 40$ K, $\log g = 4.72 \pm 0.14$, and [Fe/H] = 0.0 ± 0.1 dex. We also adopt $M_\star = 0.54 \pm 0.03\,M_\odot$ and $R_\star = 0.53 \pm 0.02\,R_\odot$ derived from the SED fitting (Sect. 3.1.1 above) that rely directly on the spectrophotometry of the star with robust empirical relations.

3.2. Polarimetry

An independent polarimetric reduction and least squares decomposition (LSD) analysis of TOI-1695 SPIRou data using the Libre-Esprit (LE) pipeline (Donati et al. 1997, 2020), leads to the polarimetric longitudinal field B_ℓ for TOI-1695 shown in Fig. C.1 and given in Table G.3. The B_ℓ measurements are consistent with those obtained in the classical APERO reduction (e.g., Martioli et al. 2022). At a given epoch, B_ℓ is directly determined from the Stokes V and Stokes I profiles (Donati et al. 1997). We find that the star has a weak polarimetric variability and magnetic activity. The Stokes V profiles have a $\chi^2_r = 0.8$ for a constant model, while the null polarization N (Donati et al. 1997) has a $\chi^2_r = 1$. Any variability in the data is thus fully consistent with the error bars.

A power spectrum of the B_ℓ data (Fig. 5) shows peaks beyond 20 days, all with a false-alarm probability (FAP) >10%. Thus, no peculiar polarimetric signal is significantly detected for TOI-1695 given the current precision. The period of ~48 days nevertheless seems to dominate the power-spectrum at low

Table 2. Spectral parameters of the star.

Parameter	Unit	TurboSpectrum+MARCS	Moog+MARCS	SED	TESS Input Catalog v8 [(f)]
$T_{\rm eff}$	K	3627±31	3711±47	3630±50	3575±157
$\log(g)$		4.60±0.05	4.53±0.13	4.5±0.5	4.723±0.009
[M/H]	dex	0.10±0.10	0.00±0.08	0.0±0.5	
$v \sin i$	km s^{-1}	<2.5 [(a)]			
$v_{\rm micro}$	km s^{-1}	fixed to 1.0	0.3±0.7		
$F_{\rm bol}$	10^{-10} erg s^{-1} cm^{-2}			6.82±0.24 [(b)]	
$L_{\rm bol}$	$L_\odot$			0.0431±0.0015 [(c)]	0.039±0.009
$M_\star$	$M_\odot$			0.54±0.03 [(d)]	0.51±0.02
$R_\star$	$R_\odot$			0.53±0.02 [(e)]	0.52±0.02

Notes. The stellar parameters are derived from spectral template matching by the method explained in Cristofari et al. (2022b) with TurboSpectrum, and in de Almeida et al. (in prep.) with Moog, from the SED fitting explained in Stassun & Torres (2016) and Stassun et al. (2017, 2018), and from the TESS project stellar parameters (Stassun et al. 2018). See Sects. 3.1.1 and 3.1.2 for details. [(a)]At 3σ and fixing $v_{\rm macro} = 0$ km s^{-1} (more details in Section 3.1.2). [(b)]From direct integration of SED. [(c)]Luminosity derived from the bolometric flux and the parallax. [(d)]Mass determined from the Mann et al. (2019) empirical relations. [(e)]Radius determined from the bolometric flux and the parallax. [(f)]From Stassun et al. (2019). See text for details.

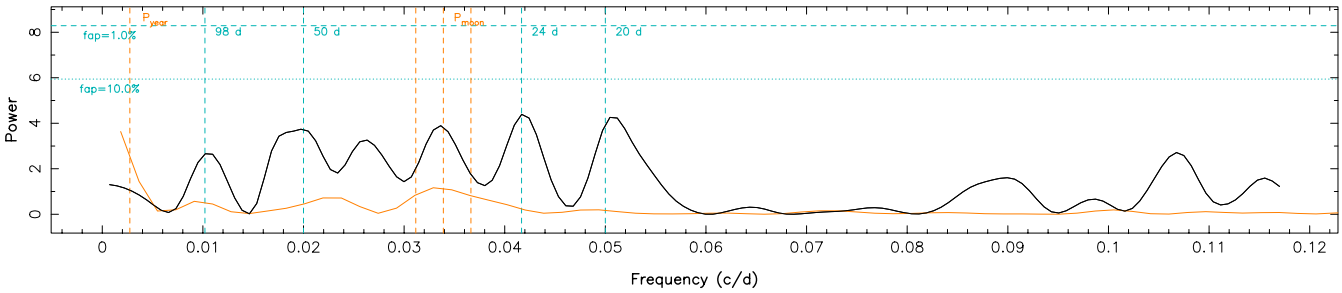

Fig. 5. Periodogram of the longitudinal magnetic field variations, with dominant frequencies highlighted in blue. The window function is shown in orange, with a peak close to the synodic orbital period of the Moon.

frequencies. We fitted the data with a quasi-periodic Gaussian process (GP; see, e.g., Haywood et al. 2014; Aigrain et al. 2015) using the same codes as in Donati et al. (2017), at an initial period of 48 days with typical decay time $\tau_{\rm decay} = 500$ days and smoothing factor $\gamma_{\rm smooth} = 0.6$. We obtain an almost flat GP model with a marginal likelihood difference $\Delta \ln \mathcal{L} = 2$ compared to a constant model. The GP model is plotted over the longitudinal field in Fig. C.1.

We can thus conclude that (i) we do not see trace of a 15-day signal, as reported in Sect. 2.1; (ii) the star was, if active, passing through a quiet phase during SPIRou observations; and (iii) more data are needed to confirm whether the hinted 48-day period could be a trace of the star's rotation signal.

3.3. RV variations and stellar activity effects

We searched for correlations between the RVs and the activity indicators, bisector span (BIS), and FWHM variations obtained from the two APERO version v6 and v7 studied in this work. The Pearson correlation coefficient for RV–BIS are $R_{\rm v6} = 0.14$ (p-value = 0.07) and $R_{\rm v7} = -0.22$ (p-value = 0.004). The Pearson correlation coefficient for RV–FWHM is $R_{\rm v6} = -0.13$ (p-value = 0.10) and $R_{\rm v7} = 0.06$ (p-value = 0.46). The only significant slope that we detect (1.7σ) is for the FWHM and RV derived from v6 of -0.62 ± 0.37 m s^{-1} per m s^{-1}. It disappears with v7 suggesting that some instrumental signal was corrected from the SPIRou data with the last implementations in the pipeline.

We thus find no significant correlations of astrophysical origin between RV and the activity indicators FWHM and BIS. This is compatible with the weak magnetic activity deduced from the almost flat longitudinal field B_ℓ.

The periodograms of the BIS and FWHM compared to the periodogram of the RVs in Fig. 6 show no significant peaks with FAP < 5% at periods <20 days, especially none at around 3.13 days, the orbital period of the candidate planet detected with TESS. Peaks with FAP < 1% appear at periods beyond 20 days, some of which coincide with large peaks of the window function.

On the other hand, in the RV periodogram we have a positive detection of the candidate planet signal at 3.13 days with a FAP ~ 1%. Two other strong peaks on both sides of this signal are due to aliases with the observing window frequencies. Most of the structures in the near periods of three days significantly weakens after fitting out a 3.13-day Keplerian to the RVs. As seen in the RV residuals periodogram in Fig. 7, residual RV variations then mainly concentrate around ~16 days. Interestingly, it is close to the 15-day period spotted in the light curve continuum variations of TESS sector 18 (Sect. 2.1). This would suggest an origin intrinsic to TOI-1695 itself or linked to its direct environment, even if no corresponding signal is detected in polarimetry. However, studies of the TOI-1695 surroundings in Sect. 2.3 exclude that the RV variations could originate from background stars at less than 3″ distance.

Inspecting the periodogram of the LBL RV derived using the APERO v7 (Fig. D.1) leads to similar conclusions. Only the power at low frequencies is significantly reduced from the RV, FWHM and the BIS variation, leaving only insignificant peaks, some of which are most likely bias of the Earth's orbital period with the ~20-day gap period. There is indeed some power at long

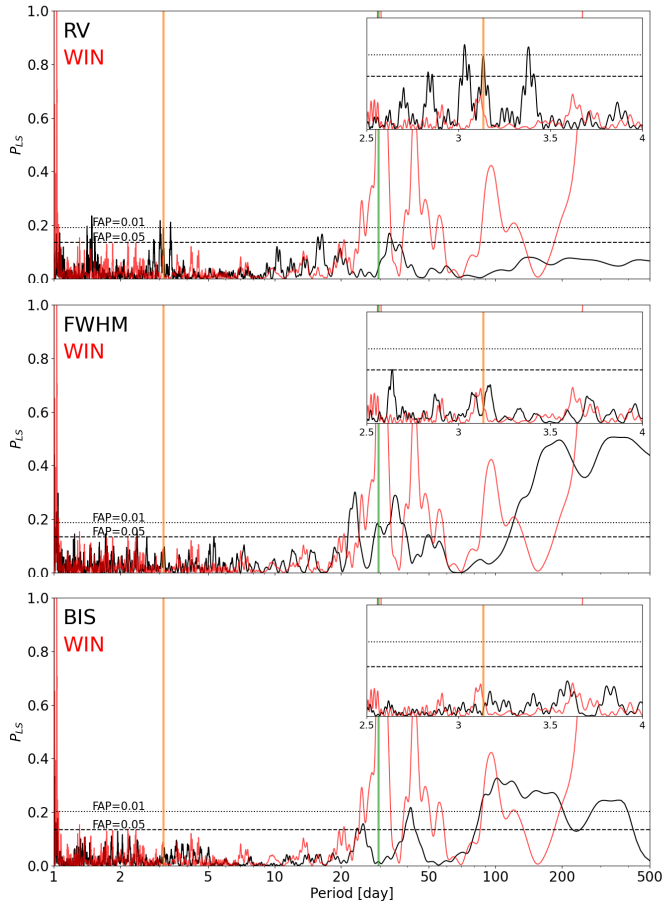

Fig. 6. Lomb-Scargle periodograms with FAP levels 0.01 and 0.05 indicated as dotted and dashed lines for data extracted with the APERO v6 version: (from top to bottom) RV, FWHM, and BIS. They are compared to the window function (red solid line). The vertical orange solid line indicates the 3.134-day period of the TESS transit signal. The moon synodic orbital period (29.53 days) is also shown as a green solid line.

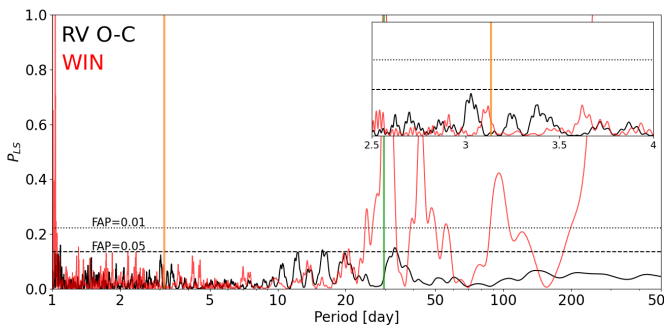

Fig. 7. Periodogram of the residuals O-C after fitting a 3.134-day Keplerian to the RVs. Same color-coding as in Fig. 6.

periods of ~365 days, which could be linked to yearly changes in the instrument resolution.

3.4. Concluding remark on the rotation period of TOI-1695

The TESS photometry and SPIRou RVs show traces of signals with periods within 14–19 days. A rotation period of the star with a period in this range would be in agreement with the M2V spectral type found for TOI-1695 (see, e.g., Goulding et al. 2012; Goulding 2013; Basri et al. 2011; Moutou et al. 2017). There are few other observations that agree or not with this stellar rotation period.

First, photometry and RV do not strictly agree with each other on the period of modulation. Photometry shows a periodogram peak at 14.8 days. The LBL RV calculated from the APERO v6 data instead show a peak at 16 days. If they are calculated from APERO v7, the peak shifts to ~18 days.

Second, if the rotation period of the star were equal to 15 days, following the hinted photometric variations in Sect. 2.1, the stellar radius of $0.53\,R_\odot$ would imply a $v \sin i$ equal to $1.8\,\mathrm{km\,s^{-1}}$, or less if the stellar spin and planet orbit are misaligned. This could agree with the $v \sin i$ of $1.9 \pm 0.2\,\mathrm{km\,s^{-1}}$ that was obtained in Sect. 3, implying in this case that the equatorial plane of the star is aligned with the orbital plane of TOI-1695 b.

Third, the SPIRou polarimetry of the star does not detect a 15-day periodicity of the star's magnetic field during the timespan of the SPIRou observations. If due to stellar rotation, we would have seen a stronger field and detected the rotational modulation in polarimetry.

Finally, we retrieved the available public photometry data to search for periodic signals indicative of stellar rotation. As of 10 September 2022, TOI-1695 was observed by the All Sky-Automated Survey for SuperNovae (ASAS-SN Shappee et al. 2014; Kochanek et al. 2017) at 2043 epochs. ASAS-SN images were obtained through a Sloan g filter (and previously, for 879 epochs, in V-band). A Lomb-Scargle periodogram analysis shows a signal at 52.4 days in V-band, but no significant signal in g-band. We also retrieved 328 and 490 epochs of photometry in Sloan g- and r-band from the Zwicky Transient Factory archive (Bellm et al. 2019; Masci et al. 2019). We find a FAP < 1% signal at 27 days in the r-band data, but not in the g-band data. In principle, the 27-day signal could be an upper harmonic of the ≈52-day signal obtained from ASAS-SN, but there is no hint of a 15-day modulation. The absence of confirmatory detections in the other bands does not allow us to draw a firm conclusion about the rotation period of TOI-1695 from these data.

We conclude that the 15-day signal seen in TESS sector 18, as well as the 16-day (or 18-day) signal seen in the SPIRou LBL RVs, are likely not related to the rotation of the star. Polarimetry, spectroscopy, photometry, and RV agree nevertheless on a star rotation period greater than 15 days. Moreover polarimetry, V-band, and r-band photometry suggest a rotation period in the range 20–52 days. Such a long rotation period is found for M dwarfs with a stellar age >1 Gyr (Engle & Guinan 2018). We thus infer that TOI-1695 is more than 1 Gyr old.

4. Joint analysis of TESS and SPIRou data

Here we use the same recipe as Martioli et al. (2022) to fit the combined photometric and velocimetric data from respectively TESS and SPIRou recorded for TOI-1695. We run a Markov chain Monte Carlo (MCMC) algorithm with the `emcee` routine (Foreman-Mackey et al. 2013) with prior distribution shown in Table 3. We fix the quadratic limb darkening parameters u_0 and u_1 with respect to Claret (2017) and Claret & Southworth (2022), for a $T_{\mathrm{eff}} = 3600$ K. We initialize 32 walkers, sample parameter space on 20 000 steps, and burn the 10 000 first samples. The posterior distributions of parameters are listed in Table 4.

We apply the fit on different analysis schemes of the LBL RV, using both v6 and v7 reductions (hereafter $\mathrm{RV_{v6}}$ and $\mathrm{RV_{v7}}$). This allows us to compare the quality of the RV series extracted from both APERO versions and to qualify the improvements brought

Table 3. Prior distribution of fitted or fixed parameters entering the MCMC sampling.

Parameter	Unit	Prior type	Prior distribution
Stellar parameters			
$M_\star$	$M_\odot$	Normal	$\mathcal{N}(0.54, 0.03)$
$R_\star$	$R_\odot$	Normal	$\mathcal{N}(0.53, 0.02)$
u_0		Fixed	0.23 [(†)]
u_1		Fixed	0.38 [(†)]
Keplerian parameters			
K	km s^{-1}	Uniform	$\mathcal{U}(0,10)$
T_0	BTJD	Uniform	$1791+\mathcal{U}(0.2,0.8)$
P	day	Uniform	$\mathcal{U}(2.51,3.76)$
a	$R_\star$	Uniform	$\mathcal{U}(10,23)$
R_p	R_J	Uniform	$\mathcal{U}(0.02,0.04)$
I_p	$^\circ$	Uniform	$\mathcal{U}(70,110)$
e		Uniform or fixed	$\mathcal{U}(0,1)$ or 0.0
ω	$^\circ$	Uniform or fixed	$\mathcal{U}(0,360)$ or 90
Gaussian process parameters			
$\sigma_\mathrm{white,phot}$	ppm	Uniform	$\mathcal{U}(-10^{100},10^{100})$
$\tau_\mathrm{decay,phot}$	day	Uniform	$\mathcal{U}(0.25,1000)$
$\gamma_\mathrm{smooth,phot}$		Uniform	$\mathcal{U}(0.1,1.5)$
P_phot	days	Uniform	$\mathcal{U}(10,20)$
A_phot	ppm	Uniform	$\mathcal{U}(10^{-4},2000)$
$\sigma_\mathrm{white,RV}$	m s^{-1}	Uniform	$\mathcal{U}(-10^{100},10^{100})$
$\tau_\mathrm{decay,RV}$	day	Uniform	$\mathcal{U}(6,1000)$
$\gamma_\mathrm{smooth,RV}$		Uniform	$\mathcal{U}(0.1,1.5)$
P_RV	days	Uniform	$\mathcal{U}(10,20)$
A_RV	m s^{-1}	Uniform	$\mathcal{U}(0,100)$

References. [(†)]Based on Claret (2017) and Claret & Southworth (2022).

by the new pipeline. For both versions, fits without drift correction nor zero-point correction were poor in terms of χ^2 and the O-C residuals. So we performed fits assuming the following:

– DC+ZPC: accounting for the long-term calibration drift of the RV and a zero-point correction (see Sect. 2 for details);

– DC+ZPC+GP: adding a quasi-periodic (QP) Gaussian process (GP) to the fit, as explained in more detail below.

The result of the joint Keplerian fit of both light curve and RVs are all compared in Table 4, assuming a circular orbit.

In the DC+ZPC scheme, the 3.134-day RV signal is found with a S/N higher than 5σ. This allows us to confirm the detection of the planet signal with a corresponding companion mass in the super-Earth-to-sub-Neptune regime $\sim 6\,M_\oplus$. Although compatible at 0.7σ, the semi-amplitude of the Keplerian model fitted to the $\mathrm{RV_{v7}}$ (3.6 ± 0.7 m s^{-1}) is smaller than that of the $\mathrm{RV_{v6}}$ (4.1 ± 0.7 m s^{-1}). On the other hand, the RV residual dispersion is slightly smaller for $\mathrm{RV_{v6}}$ than for $\mathrm{RV_{v7}}$ with respective reduced χ^2 of 0.8 and 1.1, and absolute O-C dispersion of 6 m s^{-1} and 7 m s^{-1}. We also noted a difference of $\sim$460 m s^{-1} in systemic RV, which we attributed to a different treatment of the calibration between the two versions. The difference in the Keplerian solutions and residuals, implying systematic variations unaccounted for in both, motivated us to dig further with the GP analysis of those datasets.

The quasi-periodic Gaussian process that we used combines a squared exponential (SE) and a periodic kernel with the code `george` (Ambikasaran et al. 2015) to remove the periodic pattern in the RV and the TESS-LC identified in Sects. 2.1 and 3.3. The GP is trained separately on the residual RVs and on the photometric time series excluding the transits. The priors used on the GP parameters are added to Table 3. We were careful not to allow the decay time of the SE kernel to be smaller than twice the orbital period of TOI-1695 b, thus preventing the GP from overfitting and absorbing some of the orbital signal present in the RV, along with the recommendations given in Angus et al. (2018). For optimizing the GP hyper-parameters more efficiently using an MCMC, the photometric light curves were rebinned to time steps of 0.25 days. Figures 8 and 9 show the GP modeling of the TESS light curve and the SPIRou RV.

The QP GP fit of the light curve converged to a period of $13.0^{+3.4}_{-0.7}$ days. For the $\mathrm{RV_{v6}}$ it converged to a period of $16.2^{+0.6}_{-3.9}$ days and for the $\mathrm{RV_{v7}}$ to $18.3^{+0.5}_{-4.1}$ days. After applying and then removing the GP from the RV and photometric time series, we fit again the orbital and transit signals from the RV and LC. The DC+ZPC+GP analysis leads to the smallest RV residual dispersion with reduced χ^2 of 0.6 and 0.5 respectively of $\mathrm{RV_{v6}}$ and $\mathrm{RV_{v7}}$. The flux dispersion $\sim$2008 ppm is constant over all schemes, which is not surprising given that the light curve continuum is always detrended around the transits epochs. The Bayesian information criterion (BIC) among all schemes is clearly in favor of the DC+ZPC+GP scheme with the smallest BIC. The posterior distributions although different are compatible with the DC+ZPC solutions. As expected, the model semi-amplitudes of $\mathrm{RV_{v6}}$ (3.95 ± 0.66 m s^{-1}) and $\mathrm{RV_{v7}}$ (3.63 ± 0.68 m s^{-1}) are smaller (only slightly for $\mathrm{RV_{v7}}$) than without modeling the systematic variations. The Keplerian fit of the $\mathrm{RV_{v7}}$-GP residuals leads to the best residual dispersion among all analyzed datasets, $\sigma_\mathrm{O-C} = 4.8$ m s^{-1}, but with similar planetary parameters than without fitting the GP.

As an additional check, we ran a fit of the data in the DC+ZPC scheme, but considering a nonzero eccentricity. The eccentricity obtained when letting it freely vary is consistent with 0 at 1.3σ with $e < 0.2$. More importantly, at maximum likelihood, the BIC is larger than for the zero-eccentricity case. This validates that fixing the eccentricity to zero in the other fits is the correct, most parsimonious approach, consistent with a tidally circularized orbit of the planet, and moreover does not generate significant systematic errors on the other orbital parameters.

Varying the limb darkening coefficients led to wide posterior distributions of u_0 and u_1 with unrealistic values $u_0 \sim 0.5\pm0.4$ and $u_1 \sim 0.9\pm0.7$. Although compatible within the errors with the common values assumed in the rest of the analysis, they lead to less accurate planet radius estimations with highly biased posteriors on the semimajor axis and radius. Notably, the median of the radius posterior distribution is $1.77\pm0.21\,R_\oplus$, but the maximum a posteriori point estimate is $\sim 1.99\,R_\oplus$. This shows that the present dataset is not able on its own to refine the limb darkening coefficients. It is more reasonable to rely on the known values of the limb darkening coefficients of an M 2 star.

After comparing all the different reduction and analysis schemes, we retained the solution with the smallest BIC. Finally, it is the DC+ZPC+GP derived from the APERO v7 that leads to the best solution. It can be trusted that the GP did not overfit the RV signal as the planetary parameters are similar when not fitting a GP. The corner plot of the posterior distribution of all varied and derived Keplerian parameters is shown in Fig. E.1. The best-fitting model of the transit curve is shown in Fig. 10, and the best-fitting models of the phase-folded LBL RV is shown in Fig. 11.

It results in a companion on an orbit of 3.1343 days with a planetary radius of $2.03\pm0.18\,R_\oplus$ and a planet mass of $5.5\pm1.0\,M_\oplus$. This implies a sub-Earth planet density of 3.6 ± 1.1 g cm^{-3}, and an equilibrium temperature of 590 ± 90 K.

Table 4. MCMC results of the photometry (TESS) and spectroscopy (SPIRou) joint fit.

Param.	Unit	with APERO v6		with APERO v7	
		DC+ZPC	DC+ZPC+GP	DC+ZPC	DC+ZPC+GP
Fitted parameters					
K	m s^{-1}	4.12±0.69	3.95±0.66	3.69±0.65	3.63±0.68
t_c	BTJD	1791.5205±0.0013	1791.5204±0.0013	1791.5204±0.0013	1791.5203±0.0012
P	day	3.1342788±0.0000077	3.1342793±0.0000077	3.1342788±0.0000078	3.1342790±0.0000072
a_p	$R_\star$	16.3±5.2	16.7±5.0	15.6±5.3	16.3±5.1
$R_p/R_\star$		0.0349±0.0026	0.0344±0.0025	0.0351±0.0028	0.0344±0.0027
I_c	°	89.9±3.5	89.8±3.3	90.0±3.8	89.8±3.5
u_0		0.22	0.22	0.22	0.22
u_1		0.39	0.39	0.39	0.39
γ	m s^{-1}	−59921.62±0.47	−59921.64±0.47	−59461.93±0.47	−59461.96±0.45
e		0.0	0.0	0.0	0.0
ω	°	90	90	90	90
Planet intrinsic parameters					
M_p	$M_\oplus$	6.2±1.1	6.0±1.0	5.6±1.0	5.5±1.0
R_p	$R_\oplus$	2.06±0.17	2.03±0.17	2.07±0.18	2.03±0.18
ρ_p	$\rho_\oplus$	0.71±0.22	0.71±0.21	0.63±0.20	0.66±0.21
$T_{\rm eq}$	K	580±90	575±86	590±100	590±90
$T_{\rm irr}$	K	900±140	890±130	920±160	900±140
S_p	$S_\oplus$	27±17	26±16	30±17	27±17
Goodness of fit diagnostics					
$\chi^2_{\rm r,\,RV}$		0.79	0.66	1.16	0.49
O-C$_{\rm RV}$	m s^{-1}	5.9	5.39	7.09	4.75
O-C$_{\rm phot}$	ppm	2007	2006	2010	2008
BIC		−70137	−70160	−70049	−70179
$^{(a)}\Delta$BIC		28	25	21	20
GP hyper-parameters					
$\sigma_{\rm white,phot}$	ppm		98±19		100±18
$\tau_{\rm decay,phot}$	day		$7.2^{+2.3}_{-5.1}$		$6.1^{+3.2}_{-4.7}$
$\gamma_{\rm smooth,phot}$			$0.34^{+0.11}_{-0.06}$		$0.36^{+0.15}_{-0.08}$
$P_{\rm phot}$	days		$13.0^{+3.4}_{-0.7}$		$13.0^{+4.1}_{-0.8}$
$A_{\rm phot}$	ppm		407^{+46}_{-33}		405^{+48}_{-37}
$\sigma_{\rm white,RV}$	m s^{-1}		$0.52^{+0.53}_{-0.37}$		$0.58^{+0.61}_{-0.39}$
$\tau_{\rm decay,RV}$	day		370^{+420}_{-316}		32^{+95}_{-18}
$\gamma_{\rm smooth,RV}$			$0.91^{+0.42}_{-0.50}$		$0.38^{+0.38}_{-0.16}$
$P_{\rm RV}$	days		$16.2^{+0.6}_{-3.9}$		$18.3^{+0.5}_{-4.1}$
$A_{\rm RV}$	m s^{-1}		$3.5^{+2.6}_{-1.3}$		$5.0^{+1.8}_{-1.1}$

Notes. The different RV reduction schemes using APERO v6 and v7 are presented in Sect. 4. For all parameters, except those of GPs, the main value is the median and the uncertainty is the average distance of the median to the 16th and 84th percentiles. For the GP hyper-parameters, since the posteriors are asymmetrical, the main value is given by the mode, and the uncertainties are the distance between this mode and the 16th and 84th percentiles. $^{(a)}$The ΔBIC is calculated between the model without any signal (planet or GP) and the model considered in the given column header.

5. Discussion of TOI-1695 b mass and radius

We find that TOI-1695 b is a sub-Neptune planet with an average density ~3.6 g cm^{-3} smaller than the Earth density. The mass and radius of TOI-1695 b are compared to other super-Earths and sub-Neptunes in Fig. 12, as obtained thanks to the `pyexorama` package (Zeng et al. 2021; Francesco et al. 2022). TOI-1695 b lies between two similar sub-Neptunes, Wolf-503 b (Peterson et al. 2018; Polanski et al. 2021) and TOI-270 d (Van Eylen et al. 2021; Günther et al. 2019) in terms of mass, radius, and temperature, at the border of the radius valley, but on the sub-Neptune side of it. It also has similar mass and radius to K2-3 b (Kosiarek et al. 2019), although warmer (463 K for K2-3 b).

5.1. Possible composition of the planet

We assume that a pure silicate core leads to a planet with a significant gas envelope in the formalism developed by Zeng et al. (2021). An M-R diagram comparing TOI-1695 b to other super-Earths and sub-Neptunes is shown in Fig. 12. Using the `smint` code (Piaulet et al. 2021) based on the formalism of Lopez & Fortney (2014), Zeng et al. (2016) and Aguichine et al. (2021), we considered three different scenarios:

– a planet with H–He envelope and a solid interior leads to $f_{\rm H/He} = 0.28^{+0.46}_{-0.23}$%;

– a 100% silicate interior with pure water on top of it, leads to a water envelope with a mass fraction of $f_{\rm H_2O} = 55^{+29}_{-30}$%;

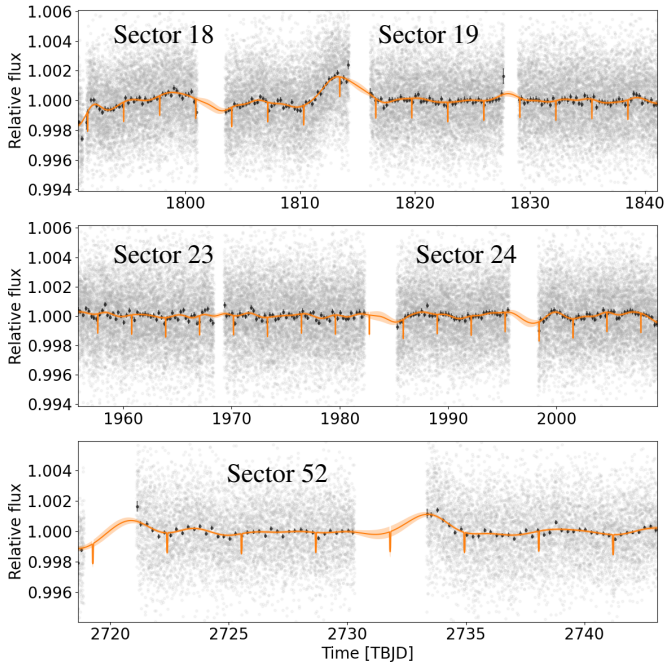

Fig. 8. Gaussian process fit of the light curve with a quasi-periodic kernel. Gray points are raw PDCSAP flux TESS data, and black points are the binned data with $\Delta t_{\rm bin} = 0.25$ days.

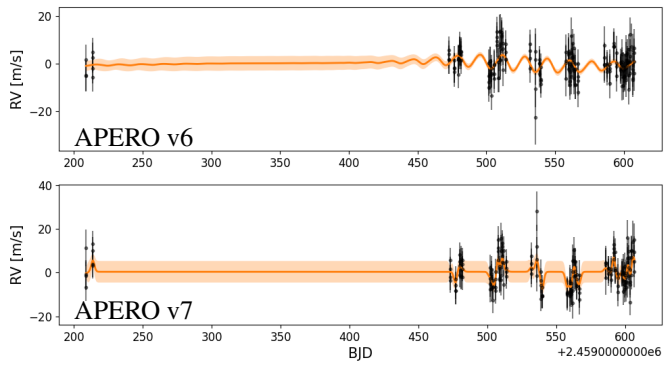

Fig. 9. Gaussian process fit of the SPIRou RV in the case of the APERO v6 reduction (top) and the v7 reduction (bottom) with a quasi-periodic kernel.

– a water-world with unfixed iron content in the core of the planet leads to an iron-to-silicate ratio $f'_{\rm core} = 47\pm30\%$ and a water envelope with a mass fraction of $f_{\rm H_2O} = 23\pm12\%$.

All of these scenarios agree on the evidence that, as for other sub-Neptune exoplanets of similar radius and mass, in particular for K2-3 b, a fraction of the planet mass should be in the form of a gaseous envelope. With $T_{\rm eq} = 590\pm90$ K, TOI-1695 b has an equilibrium temperature just below the water critical point, theoretically allowing water to be liquid if a surface pressure of about 200 atm can be sustained. However, if a significant atmospheric layer is present, the temperature will also certainly increase with pressure. Thus, water cannot be in a liquid phase on the surface of this planet, as was shown for GJ 3470 b, whose irradiation temperature is similar (Piette & Madhusudhan 2020).

5.2. Atmospheric mass loss vs. gas-depleted formation

The worlds with radius $\sim 2\,R_\oplus$ are reputed to be underabundant around solar-type stars due to atmospheric loss forming

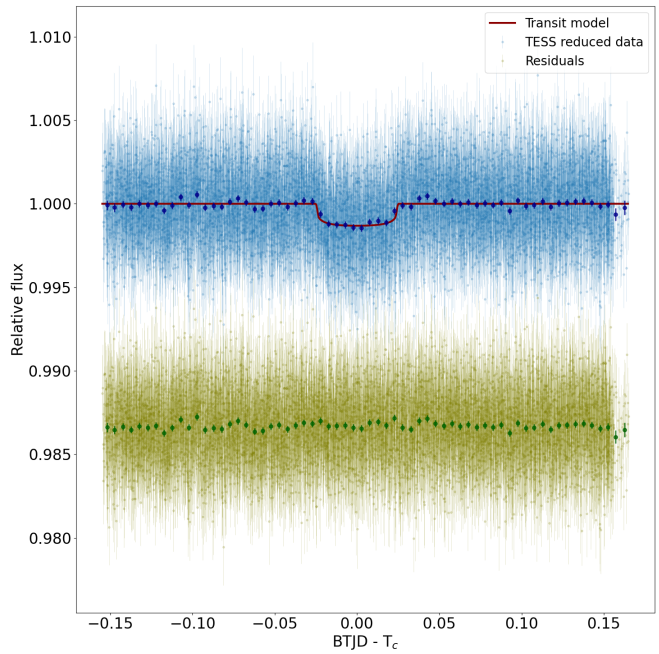

Fig. 10. Results from fits to the TESS light curve, with all the observed transits stacked, with the model taken from the maximum a posteriori point estimation, based on maximizing the posterior probability distributions for each parameter. At this point, T_0 = 1791.5206 BTJD, P = 3.1342799 days, $a = 21.1\,R_\star$, $R_p = 0.034\,R_\star$, and $I_p = 89.4°$.

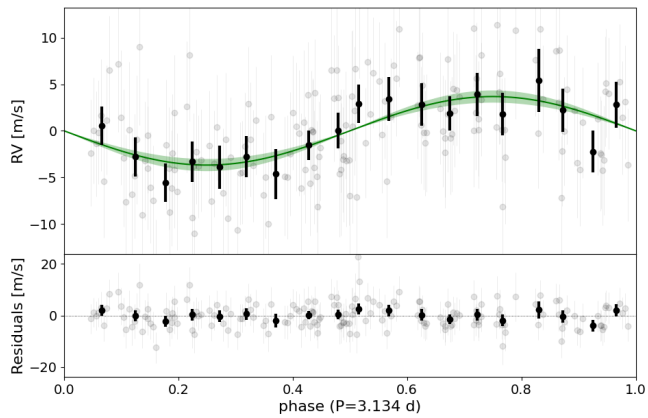

Fig. 11. Phase-folded model of the RV variation seen with SPIRou of the star TOI-1695 with a 3.13-day circular orbit. The data used here are derived from APERO v7. Gray dots gather all the RV data and black dots are binned with a time step of 0.05 days.

$R_p < 1.7\,R_\oplus$ planets (Kite & Schaefer 2021; Rogers & Owen 2021). However, TOI-1695 b, and a few others, exhibit such characteristics. Because it is located around an M dwarf, TOI-1695 b has undergone different irradiation conditions than planets around solar-type stars and has followed a different evolution with respect to photoevaporation.

Using Eq. (15) from Lecavelier Des Etangs (2007), we measure an order of magnitude for the evaporation rate for TOI-1695 b of $dm/dt \sim 10^{10}$ g s^{-1}. This evaporation rate indicates that if a H–He envelope is still present today in the atmosphere of this planet (less than 1% of the planet mass), it has to be, in this scenario, the remains of the evaporation of a much more massive envelope. If the gas represented about 10% of the mass of the initial planet, this primitive atmosphere would have had a lifetime shorter than 1.5 Gyr. This is about the minimum age of

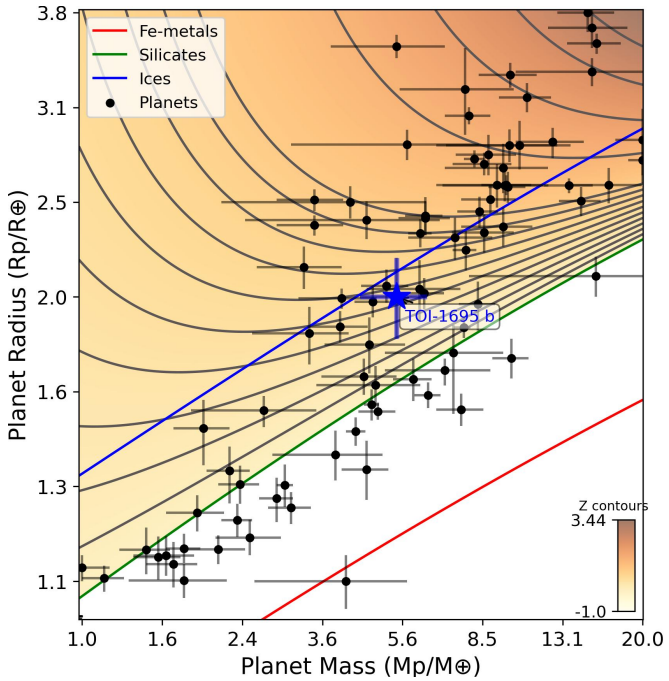

Fig. 12. Mass-radius plot obtained based on the `pyExoRaMa` code (Zeng et al. 2021; Francesco et al. 2022). The red, green, and blue solid lines represent the mass-radius relation for respectively pure Fe, silicate, and H_2O core. The yellow-brown z-contours (see Zeng et al. 2021 for details) with black solid lines represent the radius inflation due to gas in an envelope surrounding the planet core corresponding to pure silicate. The comparison planets (black circles) are taken from the TepCat database (Southworth 2011), selecting only exoplanets around M and K host stars. TOI-1695 b is shown as a blue star.

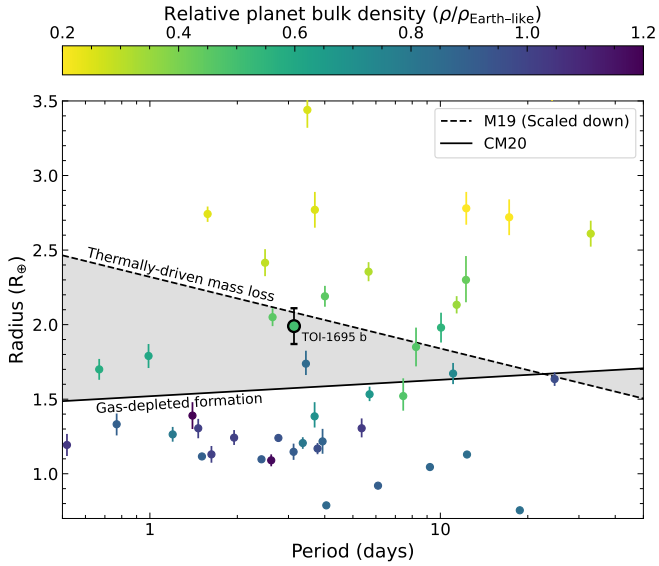

Fig. 13. R_p-$P_{\rm orb}$ diagram for exoplanets around cool stars ($T_{\rm eff}$ < 4000 K) taken from the NASA exoplanet archive. The solid and dashed lines represent respectively the Cloutier & Menou (2020) and Martinez et al. (2019) empirical radius valley (see text). The shaded region shows exoplanets that from their gas content could be able to test gas-depleted formation and thermally driven mass loss scenarios. TOI-1695 b is highlighted as a thick-lined black circle.

the system that we inferred from spectroscopic, photometric, and activity analysis of TOI-1695 in Sect. 3.

A lifetime of 10 Gyr is obtained for an envelope with 70% of the mass of the core, almost doubling the initial planet mass. Although possible, in this case the high mass loss rate requires much fine tuning of the envelope mass and the age of the planet to explain our observations. It would make this detection fortuitous, and thus unlikely if photoevaporation is responsible for the actual values of the mass and radius of TOI-1695 b.

Therefore, if the age of this system is closer to ~1 Gyr, then photoevaporation could be at the origin of a shallow H–He atmosphere; but if the age of TOI-1695 is instead beyond 5 Gyr, then this planet was more likely formed as is with a small atmosphere, and survived because it formed far away and migrated inward. In this case the scenario proposed by gas-depleted formation (Lee et al. 2014) is preferred.

This is illustrated in Fig. 13. It compares TOI-1695 b to other similar exoplanets around cool stars ($T_{\rm eff}$ < 4000 K) in an R_p-$P_{\rm orb}$ diagram and compares it to rocky and non-rocky empirical transitions consistent with gas-depleted formation (Cloutier & Menou 2020) and thermally driven atmospheric escape (Martinez et al. 2019). This includes photoevaporation (Lopez & Rice 2018) as well as core-powered mass loss (Gupta et al. 2022) mechanisms, each predicting a similar negative slope of the radius valley in R_p-$P_{\rm orb}$ space for low-mass stars. In contrast, the gas-depleted formation scenario can produce larger rocky super-Earths at longer orbital periods, resulting in a positive slope of the rocky-to-non-rocky transition. Exoplanets in the shaded region of Fig. 13 are interesting candidates to test these formation and evolution scenarios.

Determining the rocky or gaseous nature of exoplanets in the region enclosed by these two empirical R_p-$P_{\rm orb}$ relations is therefore of key importance to determining which scenario dominates over the other around M dwarfs. Here, TOI-1695 b as non-rocky tends to favor the gas-depleted formation scenario. However, it is located close to the thermally driven mass loss limit, and given the age uncertainty on the host star, the photoevaporation or core-powered mass loss scenarios cannot be rejected.

5.3. Prospect for atmospheric observations

With a J magnitude of 9.6 for the star TOI-1695, the transits of TOI-1695 b can be observed in a search for atmospheric signatures. To characterize the potential for the detection of atmospheric absorption lines, we can evaluate the ratio of the atmospheric absorption depth to the noise in the transit light curve. The noise level depends on the wavelength, telescope, instrument, for example, and the depth of the atmospheric absorption depends on the species, abundances, oscillator strength, and number of the searched lines. Therefore, now only a relative S/N of detection can be calculated for an exoplanet atmosphere to be compared with other planets to be observed for the search of the same signature with the same instrument.

Here, we made the calculation in the J-band, which is currently available from space- and ground-based facilities, and which is close to the H_2O band observed in a large number of exoplanets (e.g., Fraine et al. 2014; Benneke et al. 2019; Tsiaras et al. 2019; Mikal-Evans et al. 2021). The atmospheric absorption depth, which is the fraction of the stellar flux that is absorbed by the atmosphere during the transit, is proportional to the area of the absorbing layer, which is given by the scale height of the atmosphere (H) multiplied by $2\pi R_p$, where R_p is the planet radius, and inversely proportional to the stellar disk area ($\pi R_{\rm star}^2$). The noise is assumed to be proportional to the square root of the

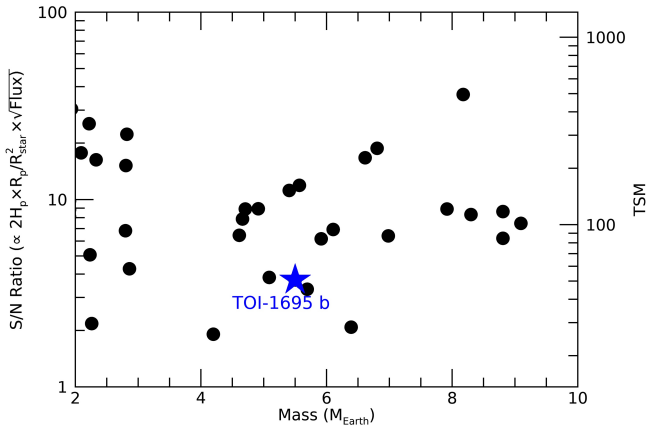

Fig. 14. Signal-to-noise ratio (left axis) of the atmospheric signatures and TSM (right axis) in the J-band as a function of the planetary mass for exoplanets orbiting M-type stars with masses between 2 and 10 Earth mass. The S/N are normalized to a reference S/N of 100 for AU Mic b, as in Martioli et al. (2022).

stellar flux given by $F_J \propto 10^{-0.4m_J}$, where m_J is the star J magnitude. The atmospheric scale height is given by $kT/\mu g$, where T is the atmosphere temperature, k the Boltzmann constant, μ the mean molar molecular mass, and g is the planet gravity. Finally, with $g \propto M_p/R_p^2$, where M_p is the mass of the planet, the signal-to-noise ratio is given by $S/N \propto HR_p/R_{\rm star}^2\sqrt{F_J}$, in agreement with the transmission spectroscopic metric (TSM) as defined by Kempton et al. (2018, see also Cointepas et al. 2021).

We calculated the S/N expected for all known exoplanets transiting an M star, and normalized them to the value of 100 for AU Mic b, as done in Martioli et al. (2022). We used the catalog of exoplanets published in the Exoplanets Encyclopedia on 18 July 2022 (Schneider et al. 2011). For the J magnitudes, we used the tabulated values when available or calculated theoretical values from the V magnitudes and the stars' effective temperatures assuming a blackbody spectrum. We considered only the M-type stars in the catalog; a star is considered to be an M-type if it is tabulated with this stellar type or if no stellar type is given in the catalog and its effective temperature is between 2200 and 3900 K.

The result is shown in Fig. 14 where we plotted the S/N of the atmospheric signatures and the TSM in the J-band as a function of the planetary mass for known exoplanets orbiting M-type stars with masses between 2 and 10 $M_\oplus$. With an S/N of 4 of TOI-1695 b, in the 2–10 Earth mass range, several exoplanets yield a much better S/N. Even if we calculate the same plot for the S/N in the V-band, with a stellar type M2V and a V magnitude of 13.0, the situation is barely improved and the conclusion remains the same. Nevertheless, TOI-1695 b has a TSM of 48, a decent S/N to be reached in only 10 h of observation with JWST.

We also determined the emission signature metric (ESM; Eq. (4) in Kempton et al. 2018) of TOI-1695 b in the K-band, assuming a day-side temperature of the planet of $1.1\times T_{\rm eq}$. We found an ESM of 3, implying an $S/N = 3$ for a JWST detection of the planet in the K-band during a secondary eclipse. This is again significantly below the threshold for defining the best emission targets, but still challenging in term of detectability.

Thus, even though TOI-1695 b is not the best target in terms of precision, its atmosphere could still be characterized with a limited observation time on large telescopes such as JWST.

6. Summary and conclusion

Thanks to RV follow-up observations with SPIRou at CFHT, we have established the planetary nature of a companion discovered by TESS around the star TOI-1695 with an orbital period of 3.134 days.

We showed that TOI-1695 b is a sub-Neptune planet, with a mass of 5.5±1.0 $M_\oplus$ and a radius of 2.03±0.18 $R_\oplus$. We found hints of a supplementary weak variability in both photometry (P∼12–15 days) and RV (P∼16–19 days), but not present in activity indicators (polarimetry, FWHM, bisector span). These activity indicators moreover do not show signs of any clear modulation below a period of ∼20 days. It implies that TOI-1695 is likely to be a slow rotator, older than 1 Gyr. The origin of the supplementary variability in RV and photometry is still uncertain.

The density of TOI-1695 b is 3.6±1.1 g cm^{-3}, which suggests the existence of an atmospheric layer on top of the solid bulk of the planet. If made of H–He, the gas envelope would have a low mass fraction $f_{\rm H/He} = 0.28^{+0.46}_{-0.12}\%$. If containing water and varying its core composition, the planet may have a water mass fraction of 23±12%. This confirms that TOI-1695 b lies in the sub-Neptune domain of the radius valley.

The detection prospects of the atmosphere of TOI-1695 b with current and future instruments, such as the JWST and ELTs, with a TSM of 48 are relatively encouraging. Its atmosphere has a S/N of detection lower than several other similar targets, and its characterization is thus not the easiest. Nevertheless, its radius and orbital period compared to the rocky-to-gaseous bounds of the different formation and evolution scenarios of super-Earths and sub-Neptunes make it an interesting case for testing these scenarios.

Acknowledgements. The authors gratefully thank the anonymous referee for his corrections and suggestions that led to improve the content of this article. The authors wish to recognize and acknowledge the very significant cultural role and reverence that the summit of MaunaKea has always had within the indigenous Hawaiian community. We are most fortunate to have the opportunity to conduct observations from this mountain. This paper includes data collected by the TESS mission, which are publicly available from the Mikulski Archive for Space Telescopes (MAST). Funding for the TESS mission is provided by NASA's Science Mission directorate. S.T.Sc.I. is operated by the Association of Universities for Research in Astronomy, Inc., under NASA contract NAS 5-26555. We acknowledge funding from the French National Research Agency (ANR) under contract number ANR18CE310019 (SPlaSH). F.K. acknowledges support from the Université Paris Sciences et Lettres under the DIM-ACAV program Origines et conditions d'apparition de la vie. E.M. acknowledges funding from the Fundação de Amparo à Pesquisa do Estado de Minas Gerais (FAPEMIG) under the project number APQ-02493-22. J.-F.D. acknowledges funding from the European Research Council (ERC) under the H2020 research & innovation programme (grant agreement #740651 NewWorlds). This work is partly supported by the French National Research Agency in the framework of the Investissements d'Avenir program (ANR-15-IDEX-02), through the funding of the "Origin of Life" project of the Grenoble-Alpes University. J.H.C.M. is supported in the form of a work contract funded by Fundação para a Ciência e Tecnologia (FCT) with the reference DL 57/2016/CP1364/CT0007; and also supported from FCT through national funds and by FEDER-Fundo Europeu de Desenvolvimento Regional through COMPETE2020-Programa Operacional Competitividade e Internacionalização for these grants UIDB/04434/2020 & UIDP/04434/2020, PTDC/FIS-AST/32113/2017 & POCI-01-0145-FEDER-032113, PTDC/FIS-AST/28953/2017 & POCI-01-0145-FEDER-028953, PTDC/FIS-AST/29942/2017. J.H.C.M. also acknowleges the support from FCT - Fundação para a Ciência e a Tecnologia through national funds and by FEDER through COMPETE2020 - Programa Operacional Competitividade e Internacionalização by these grants: UID/FIS/04434/2019; UIDB/04434/2020; UIDP/04434/2020; PTDC/FIS-AST/32113/2017 & POCI-01-0145-FEDER-032113; PTDC/FIS-AST/28953/2017 & POCI-01-0145-FEDER-028953.

References

Aguichine, A., Mousis, O., Deleuil, M., & Marcq, E. 2021, ApJ, 914, 84
Aigrain, S., Llama, J., Ceillier, T., et al. 2015, MNRAS, 450, 3211
Ambikasaran, S., Foreman-Mackey, D., Greengard, L., Hogg, D. W., & O'Neil, M. 2015, IEEE Trans. Pattern Anal. Mach. Intell., 38, 252
Angus, R., Morton, T., Aigrain, S., Foreman-Mackey, D., & Rajpaul, V. 2018, MNRAS, 474, 2094
Artigau, É., Astudillo-Defru, N., Delfosse, X., et al. 2014, SPIE Conf. Ser., 9149, 914905
Artigau, É., Cadieux, C., Cook, N. J., et al. 2022, AJ, 164, 84
Asplund, M., Grevesse, N., Sauval, A. J., & Scott, P. 2009, ARA&A, 47, 481
Basri, G., Walkowicz, L. M., Batalha, N., et al. 2011, AJ, 141, 20
Bellm, E. C., Kulkarni, S. R., Graham, M. J., et al. 2019, PASP, 131, 018002
Benneke, B., Wong, I., Piaulet, C., et al. 2019, ApJ, 887, L14
Blanco-Cuaresma, S. 2019, MNRAS, 486, 2075
Bouchy, F., Pepe, F., & Queloz, D. 2001, A&A, 374, 733
Cadieux, C., Doyon, R., Plotnykov, M., et al. 2022, AJ, 164, 96
Ciardi, D. R., Beichman, C. A., Horch, E. P., & Howell, S. B. 2015, ApJ, 805, 16
Claret, A. 2017, A&A, 600, A30
Claret, A., & Southworth, J. 2022, A&A, 664, A128
Cloutier, R., & Menou, K. 2020, AJ, 159, 211
Cutri, R.-M., Skrutskie, M.-F., van Dyk, S., et al. 2003, in 2MASS All-Sky Point Source Catalog, NASA/IPAC Infrared Science Archive
Cointepas, M., Almenara, J. M., Bonfils, X., et al. 2021, A&A, 650, A145
Cook, N. J., Artigau, É., Doyon, R., et al. 2022, PASP, 134, 114509
Cristofari, P. I., Donati, J. F., Masseron, T., et al. 2022a, MNRAS, 516, 3802
Cristofari, P. I., Donati, J. F., Masseron, T., et al. 2022b, MNRAS, 511, 1893
Donati, J. F., Semel, M., Carter, B. D., Rees, D. E., & Collier Cameron, A. 1997, MNRAS, 291, 658
Donati, J. F., Yu, L., Moutou, C., et al. 2017, MNRAS, 465, 3343
Donati, J. F., Kouach, D., Moutou, C., et al. 2020, MNRAS, 498, 5684
Engle, S. G., & Guinan, E. F. 2018, Res. Notes Am. Astron. Soc., 2, 34
Foreman-Mackey, D., Hogg, D. W., Lang, D., & Goodman, J. 2013, PASP, 125, 306
Fraine, J., Deming, D., Benneke, B., et al. 2014, Nature, 513, 526
Francesco, A., Mario, D., Li, Z., & Alessandro, S. 2022, Res. Notes Am. Astron. Soc., 6, 28
Fulton, B. J., & Petigura, E. A. 2018, AJ, 156, 264
Fulton, B. J., Petigura, E. A., Howard, A. W., et al. 2017, AJ, 154, 109
Furlan, E., Ciardi, D. R., Everett, M. E., et al. 2017, AJ, 153, 71
Gaia Collaboration (Brown, A. G. A. et al.) 2021, A&A, 649, A1
Giacalone, S., & Dressing, C. D. 2020, Astrophysics Source Code Library [record ascl:2002.004]
Giacalone, S., Dressing, C. D., Jensen, E. L. N., et al. 2021, AJ, 161, 24
Ginzburg, S., Schlichting, H. E., & Sari, R. 2018, MNRAS, 476, 759
Goulding, N. T. 2013, PhD thesis, University of Hertfordshire, UK
Goulding, N. T., Barnes, J. R., Pinfield, D. J., et al. 2012, MNRAS, 427, 3358
Günther, M. N., Pozuelos, F. J., Dittmann, J. A., et al. 2019, Nat. Astron., 3, 1099
Gupta, A., Nicholson, L., & Schlichting, H. E. 2022, MNRAS, 516, 4585
Gustafsson, B., Edvardsson, B., Eriksson, K., et al. 2008, A&A, 486, 951
Hauschildt, P. H., Allard, F., & Baron, E. 1999, ApJ, 512, 377
Haywood, R. D., Collier Cameron, A., Queloz, D., et al. 2014, MNRAS, 443, 2517
Hobson, M. J., Bouchy, F., Cook, N. J., et al. 2021, A&A, 648, A48
Jenkins, J. M., Twicken, J. D., McCauliff, S., et al. 2016, SPIE Conf. Ser., 9913, 99133E
Kanodia, S., & Wright, J. 2018, Res. Notes Am. Astron. Soc., 2, 4
Kempton, E. M. R., Bean, J. L., Louie, D. R., et al. 2018, PASP, 130, 114401
Kite, E. S., & Schaefer, L. 2021, ApJ, 909, L22
Kochanek, C. S., Shappee, B. J., Stanek, K. Z., et al. 2017, PASP, 129, 104502
Kosiarek, M. R., Crossfield, I. J. M., Hardegree-Ullman, K. K., et al. 2019, AJ, 157, 97
Kovács, G., Zucker, S., & Mazeh, T. 2002, A&A, 391, 369
Kreidberg, L. 2015, PASP, 127, 1161
Lecavelier Des Etangs, A. 2007, A&A, 461, 1185
Lee, E. J., & Connors, N. J. 2021, ApJ, 908, 32
Lee, E. J., Chiang, E., & Ormel, C. W. 2014, ApJ, 797, 95
Li, J., Tenenbaum, P., Twicken, J. D., et al. 2019, PASP, 131, 024506
Lightkurve Collaboration (Cardoso, J. V. d. M., et al.) 2018, Astrophysics Source Code Library [record ascl:1812.013]
Lopez, E. D., & Fortney, J. J. 2014, ApJ, 792, 1
Lopez, E. D., & Rice, K. 2018, MNRAS, 479, 5303
Mann, A. W., Dupuy, T., Kraus, A. L., et al. 2019, ApJ, 871, 63
Martinez, C. F., Cunha, K., Ghezzi, L., & Smith, V. V. 2019, ApJ, 875, 29
Martioli, E., Hébrard, G., Moutou, C., et al. 2020, A&A, 641, L1
Martioli, E., Hébrard, G., Fouqué, P., et al. 2022, A&A, 660, A86
Masci, F. J., Laher, R. R., Rusholme, B., et al. 2019, PASP, 131, 018003
McQuillan, A., Aigrain, S., & Roberts, S. 2012, A&A, 539, A137
Mikal-Evans, T., Crossfield, I. J. M., Benneke, B., et al. 2021, AJ, 161, 18
Montegriffo, P., De Angeli, F., Andrae, R., et al. 2023, A&A, in press, https://doi.org/10.1051/0004-6361/202243880
Moutou, C., Hébrard, E. M., Morin, J., et al. 2017, MNRAS, 472, 4563
Muirhead, P. S., Dressing, C. D., Mann, A. W., et al. 2018, AJ, 155, 180
Owen, J. E., & Wu, Y. 2013, ApJ, 775, 105
Passegger, V. M., Schweitzer, A., Shulyak, D., et al. 2019, A&A, 627, A161
Peterson, M. S., Benneke, B., David, T. J., et al. 2018, AJ, 156, 188
Piaulet, C., Benneke, B., Rubenzahl, R. A., et al. 2021, AJ, 161, 70
Piette, A. A. A., & Madhusudhan, N. 2020, ApJ, 904, 154
Plez, B. 2012, Astrophysics Source Code Library [record ascl:1205.004]
Polanski, A. S., Crossfield, I. J. M., Burt, J. A., et al. 2021, AJ, 162, 238
Ricker, G. R., Winn, J. N., Vanderspek, R., et al. 2015, J. Astron. Teles. Instrum. Syst., 1, 014003
Rogers, J. G., & Owen, J. E. 2021, MNRAS, 503, 1526
Schlegel, D. J., Finkbeiner, D. P., & Davis, M. 1998, ApJ, 500, 525
Schneider, J., Dedieu, C., Le Sidaner, P., Savalle, R., & Zolotukhin, I. 2011, A&A, 532, A79
Shappee, B. J., Prieto, J. L., Grupe, D., et al. 2014, ApJ, 788, 48
Shuvalov, V. 2009, MAPS, 44, 1095
Smith, J. C., Stumpe, M. C., Van Cleve, J. E., et al. 2012, PASP, 124, 1000
Smith, V. V., Bizyaev, D., Cunha, K., et al. 2021, AJ, 161, 254
Sneden, C., Bean, J., Ivans, I., Lucatello, S., & Sobeck, J. 2012, Astrophysics Source Code Library [record ascl:1202.009]
Southworth, J. 2011, MNRAS, 417, 2166
Stassun, K. G., & Torres, G. 2016, AJ, 152, 180
Stassun, K. G., & Torres, G. 2021, ApJ, 907, L33
Stassun, K. G., Collins, K. A., & Gaudi, B. S. 2017, AJ, 153, 136
Stassun, K. G., Corsaro, E., Pepper, J. A., & Gaudi, B. S. 2018, AJ, 155, 22
Stassun, K. G., Oelkers, R. J., Paegert, M., et al. 2019, AJ, 158, 138
Stumpe, M. C., Smith, J. C., Catanzarite, J. H., et al. 2014, PASP, 126, 100
Tsiaras, A., Waldmann, I. P., Tinetti, G., Tennyson, J., & Yurchenko, S. N. 2019, Nat. Astron., 3, 1086
Twicken, J. D., Catanzarite, J. H., Clarke, B. D., et al. 2018, PASP, 130, 064502
Van Eylen, V., Agentoft, C., Lundkvist, M. S., et al. 2018, MNRAS, 479, 4786
Van Eylen, V., Astudillo-Defru, N., Bonfils, X., et al. 2021, MNRAS, 507, 2154
Wizinowich, P., Acton, D. S., Shelton, C., et al. 2000, PASP, 112, 315
Wright, J. T., & Eastman, J. D. 2014, PASP, 126, 838
Wright, E. L., Eisenhard, P. R. M., Mainzer, A. K., et al. 2010, AJ, 140, 1868
Wu, Y. 2019, ApJ, 874, 91
Zeng, L., Sasselov, D. D., & Jacobsen, S. B. 2016, ApJ, 819, 127
Zeng, L., Jacobsen, S. B., Hyung, E., et al. 2021, ApJ, 923, 247

[1] LESIA, Observatoire de Paris, Université PSL, CNRS, Sorbonne Université, Université Paris Cité, 5 place Jules Janssen, 92195 Meudon, France
e-mail: flavien.kiefer@obspm.fr
[2] Sorbonne Université, CNRS, UMR 7095, Institut d'Astrophysique de Paris, 98 bis bd Arago, 75014 Paris, France
[3] Observatoire de Haute-Provence, CNRS, Université d'Aix-Marseille, 04870 Saint-Michel-l'Observatoire, France
[4] Laboratório Nacional de Astrofísica, Rua Estados Unidos 154, 37504-364 Itajubá - MG, Brazil
[5] Université de Montréal, Département de Physique, IREX, Montréal, QC H3C 3J7, Canada
[6] Institut de Recherche en Astrophysique et Planétologie, Université de Toulouse, CNRS, IRAP/UMR 5277, 14 avenue Edouard Belin, 31400 Toulouse, France
[7] CNRS, IPAG, Université Grenoble Alpes, F-38000 Grenoble, France
[8] NASA Exoplanet Science Institute, Caltech/IPAC, Pasadena, CA 91125, USA
[9] Department of Astronomy and Astrophysics, University of California, Santa Cruz, CA 95064, USA
[10] Department of Physics and Astronomy, Vanderbilt University, Nashville, TN 37235, USA
[11] Instituto de Astrofísica e Ciencias do Espaço, Universidade do Porto, CAUP, Rua das Estrelas, 4150-762 Porto, Portugal
[12] European Southern Observatory, Alonso de Cordova, Vitacura, Santiago, Chile

[13] Canada-France-Hawaii Telescope, CNRS, 96743 Kamuela, Hawaii, USA
[14] Institut de Recherche sur les Exoplanètes, Département de Physique, Université de Montréal, 1375 Avenue Thérèse-Lavoie-Roux, Montréal, QC H2V 0B3, Canada
[15] Aix-Marseille Univ., CNRS, CNES, Institut Origines, LAM, Marseille, France
[16] Department of Physics and Kavli Institute for Astrophysics and Space Research, Massachusetts Institute of Technology, Cambridge, MA 02139, USA
[17] Space Telescope Science Institute, 3700 San Martin Drive, Baltimore, MD, 21218, USA
[18] Center for Astrophysics, Harvard & Smithsonian, 60 Garden St, Cambridge, MA 02138, USA
[19] MIT Kavli Institute for Astrophysics and Space Research, Massachusetts Institute of Technology, Cambridge, MA 02139, USA
[20] Earth and Planetary Sciences, Massachusetts Institute of Technology, 77 Massachusetts Avenue, Cambridge, MA 02139, USA
[21] Department of Aeronautics and Astronautics, MIT, 77 Massachusetts Avenue, Cambridge, MA 02139, USA
[22] NASA Ames Research Center, Moffett Field, CA 94035, USA
[23] SETI Institute, Mountain View, CA 94043, USA
[24] Department of Astrophysical Sciences, Peyton Hall, 4 Ivy Lane, Princeton, NJ 08544, USA
[25] Instituto de Astrofísica e Ciências do Espaço, Universidade do Porto, CAUP, Rua das Estrelas, 4150-762 Porto, Portugal
[26] LATMOS/IPSL, UVSQ Université Paris-Saclay, Sorbonne Université, CNRS, 78280 Guyancourt, France
[27] Institute of Astronomy and Astrophysics, Academia Sinica, Taipei 10617, Taiwan
[28] Department of Earth Sciences, University of Hawaii at Manoa, Honolulu, Hawaii 96822 USA
[29] Konkoly Observatory, Research Centre for Astronomy and Earth Sciences, Eötvös Loránd Research Network (ELKH), Konkoly-Thege Miklós út 15-17, 1121 Budapest, Hungary
[30] CSFK, MTA Centre of Excellence, Budapest, Konkoly Thege Miklós út 15-17, 1121, Hungary
[31] Max-Planck-Institute for Astronomy, Königstuhl 17, 69117 Heidelberg, Germany
[32] ELTE Eötvös Loránd University, Institute of Physics, Pázmány Péter sétány 1/A, 1117 Budapest, Hungary
[33] Universidade Federal do Rio Grande do Norte (UFRN), 59078-970, Natal, RN, Brazil
[34] Center for Astrophysics, Harvard & Smithsonian, 60 Garden Street, Cambridge, MA 02138, USA

Appendix A: TESS aperture and field of view

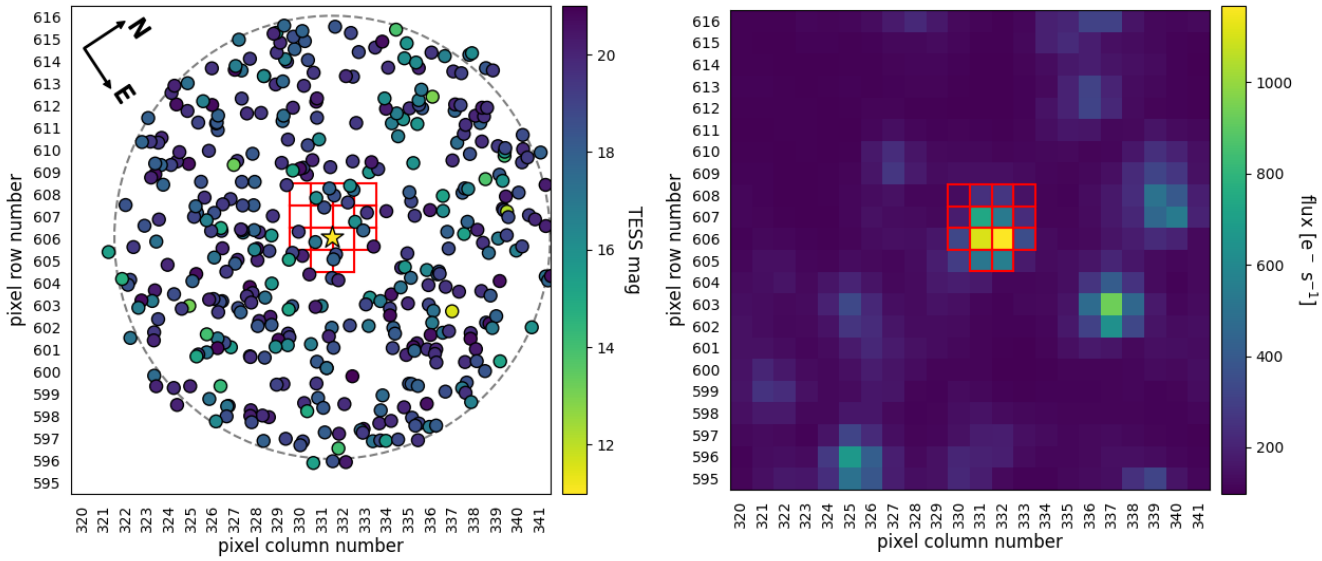

Fig. A.1. Aperture used to retrieve the photometry of TOI-1695 from the SPOC in sector 18, compared to the background sources identified by *Gaia* within 200″ (left), and the background resolved sources on the full-frame image (right). This image is an output from TRICERATOPS (see text).

Appendix B: Spectral model of the star

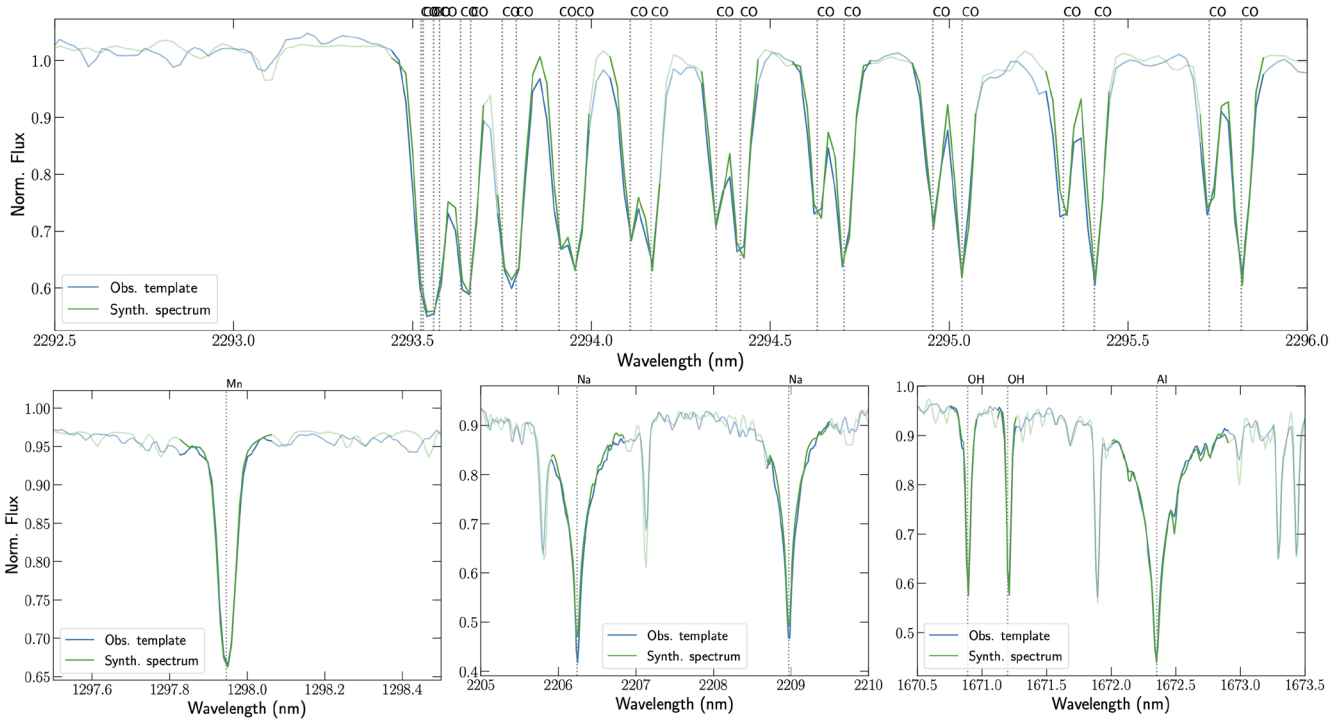

Fig. B.1. Stellar line spectral fitting with the MARCS model (see Section 3 for explanations), with CO (top), Mn (bottom left), Na (bottom middle), and OH (bottom right) lines. The best-fitting model is plotted as a green solid line.

Appendix C: SPIRou polarimetry time series

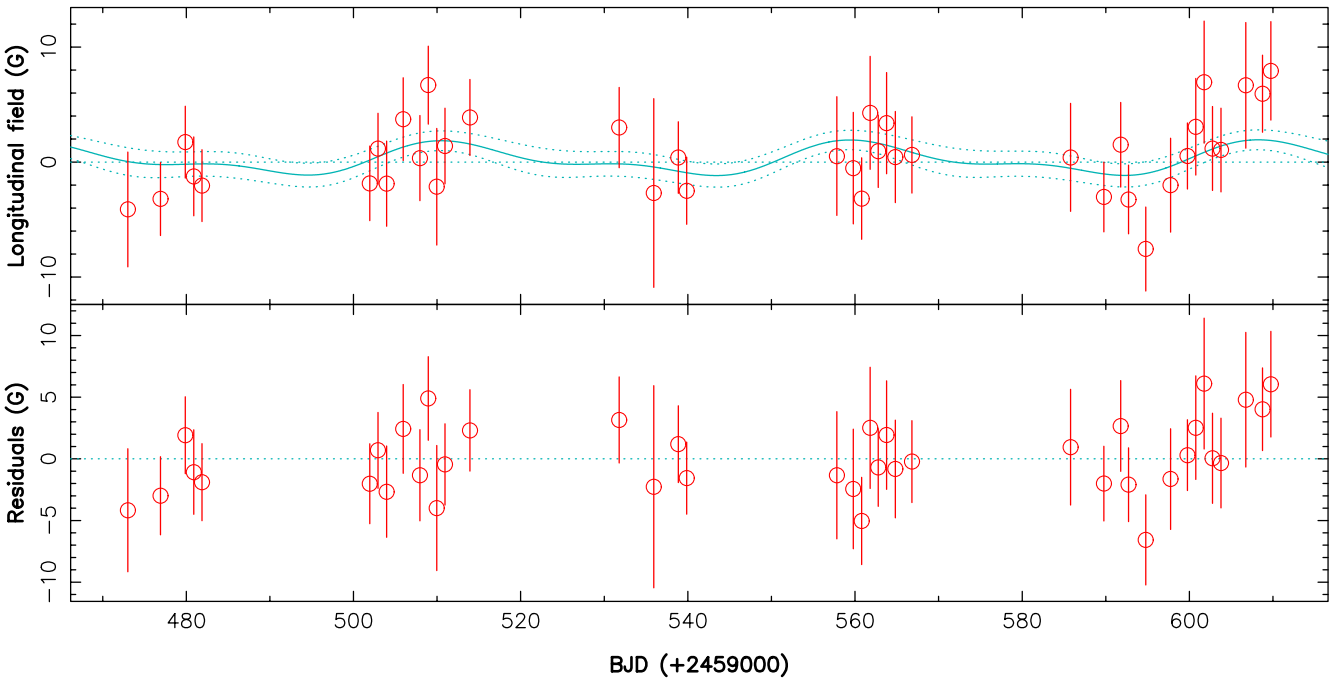

Fig. C.1. Longitudinal magnetic field variations (red points). A Gaussian process best fit with a period of 48 d with a decay time of 500 days and a smoothing factor commonly fixed to 0.6 days is also shown in blue.

Appendix D: Periodograms of RV, FWHM, and BIS obtained with APERO v7

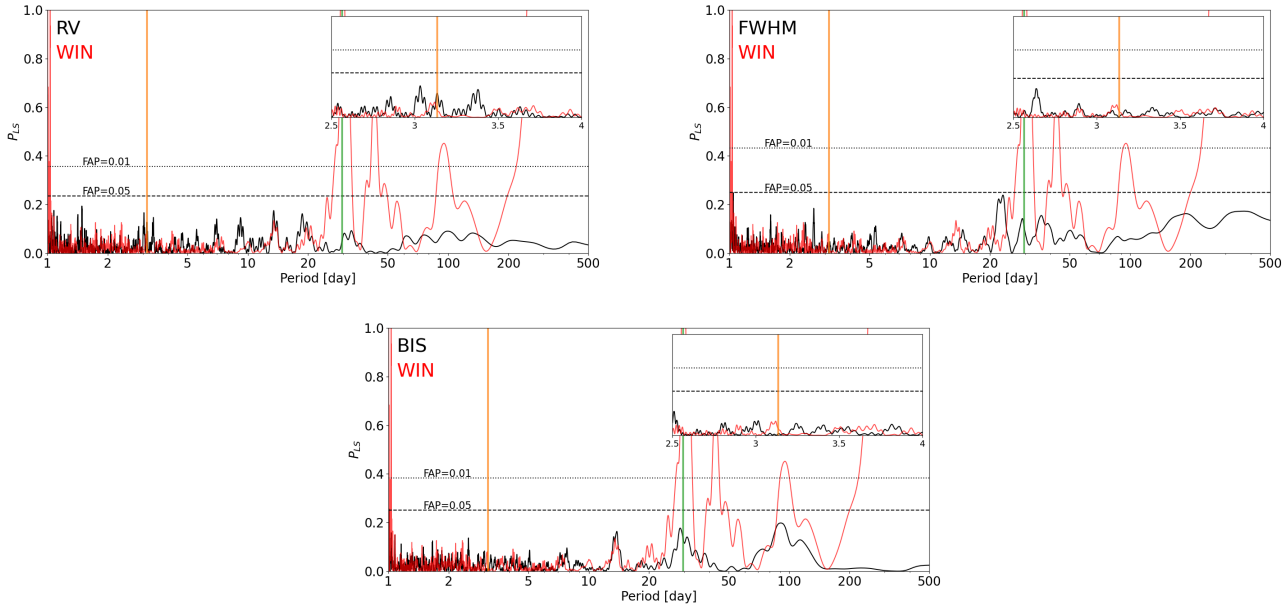

Fig. D.1. Same as Fig. 6, but obtained with APERO v7.

Appendix E: Corner plot of the MCMC posterior distributions for the transit and RV fit

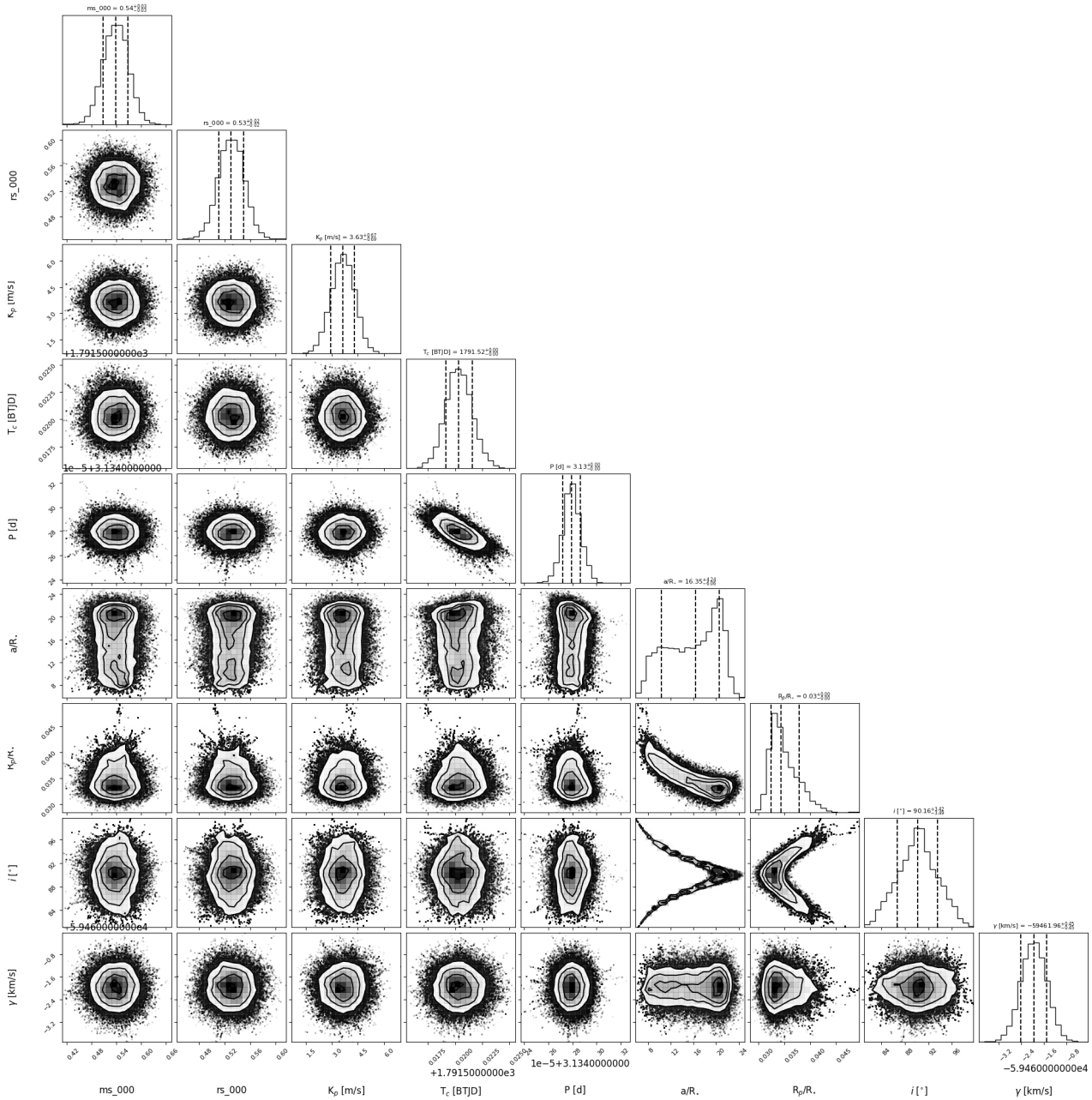

Fig. E.1. MCMC fit posteriors of SPIRou and TESS data. The scheme used is where RVs are drift corrected (DC) and zero-point corrected (ZPC), and a GP with $P_{\rm GP}$=14.8 days is fitted from the RVs and the light curve. The blue solid line indicates the median of the posterior probability density function (pdf), and the black dotted lines locate the 16 and 84 percentiles of the posterior pdf.

Appendix F: Observation logs.

Table F.1. Log of SPIRou observations of TOI-1695. The dagger (†) indicates data that were excluded from the drift corrected data reduced with APERO v6. The star (⋆) indicates data removed from the drift corrected and zero point corrected data reduced with APERO v7 (see discussion in Section 2).

Epoch	UT Date	BJD -2,459,000	BERV (km s^{-1})	Exp. time (sec)	Airmass	S/N at 1670 nm	H_2O rel. abs.	Moon up?	Moon angle (°)	Moon phase	Pol. seq. number
1	2020-12-25T07:09:48	208.794938	-9.5505	1204	1.69	142	4.17	T	62	0.80	1
1	2020-12-25T07:30:20	208.809194	-9.5649	1204	1.71	140	4.36	T	62	0.80	2
1	2020-12-25T07:50:52	208.823449	-9.5787	1204	1.75	145	4.54	T	62	0.80	3
1	2020-12-25T08:11:23	208.837704	-9.5920	1204	1.79	141	4.62	T	62	0.80	4
2	2020-12-30T06:17:47	213.758646	-10.7086	1204	1.66	135	2.10	T	64	-1.00	1
2	2020-12-30T06:38:19	213.772901	-10.7233	1204	1.68	135	2.20	T	64	-1.00	2
2	2020-12-30T06:58:50	213.787157	-10.7376	1204	1.70	137	2.25	T	64	-1.00	3
2	2020-12-30T07:19:22	213.801412	-10.7516	1204	1.73	133	2.40	T	64	-1.00	4
3	2021-09-15T11:39:36	472.980910	15.1838	1204	1.67	142	2.10	F	117	0.77	1
3	2021-09-15T12:00:07	472.995168	15.1704	1204	1.65	145	2.11	F	117	0.77	2
3	2021-09-15T12:20:33	473.009361	15.1570	1204	1.65	145	2.12	F	117	0.77	3
3	2021-09-15T12:40:59	473.023551	15.1436	1204	1.65	147	2.09	F	117	0.77	4
4	2021-09-19T09:19:11	476.883601	14.7815	1204	1.90	148	3.08	T	90	0.97	1
4	2021-09-19T09:39:37	476.897791	14.7706	1204	1.84	152	3.09	T	91	0.97	2
4	2021-09-19T10:00:09	476.912048	14.7589	1204	1.79	150	3.04	T	89	0.97	3
4	2021-09-19T10:20:35	476.926239	14.7468	1204	1.75	152	2.80	T	89	0.97	4
5	2021-09-22T08:51:52	479.864766	14.3903	1204	1.95	155	1.22	T	70	-0.98	1
5	2021-09-22T09:12:23	479.879022	14.3797	1204	1.89	156	1.20	T	70	-0.98	2
5	2021-09-22T09:32:49	479.893215	14.3684	1204	1.83	153	1.12	T	70	-0.98	3
5	2021-09-22T09:53:15	479.907407	14.3565	1204	1.78	153	1.06	T	70	-0.98	4
6	2021-09-23T09:02:08	480.871949	14.2419	1204	1.91	150	4.95	T	65	-0.94	1
6	2021-09-23T09:22:40	480.886206	14.2308	1204	1.84	148	4.74	T	65	-0.94	2
6	2021-09-23T09:43:06	480.900398	14.2190	1204	1.79	146	3.13	T	65	-0.94	3
6	2021-09-23T10:03:32	480.914590	14.2067	1204	1.75	143	4.74	T	64	-0.94	4
7	2021-09-24T08:40:33	481.857005	14.1059	1204	1.97	154	1.61	T	61	-0.88	1
7	2021-09-24T09:00:59	481.871199	14.0953	1204	1.90	150	1.58	T	60	-0.88	2
7	2021-09-24T09:21:25	481.885388	14.0840	1204	1.84	153	1.54	T	60	-0.88	3
7	2021-09-24T09:41:51	481.899581	14.0721	1204	1.79	153	1.46	T	60	-0.88	4
8	2021-10-14T10:23:45	501.929496	10.2267	1204	1.65	152	3.84	T	106	0.73	1
8	2021-10-14T10:44:17	501.943753	10.2116	1204	1.65	149	3.85	T	106	0.73	2
8	2021-10-14T11:04:49	501.958010	10.1966	1204	1.65	148	4.00	T	106	0.73	3
8	2021-10-14T11:25:15	501.972201	10.1818	1204	1.66	153	4.05	F	106	0.73	4
9	2021-10-15T10:03:28	502.915441	10.0123	1204	1.65	156	2.77	T	98	0.73	1
9	2021-10-15T10:24:00	502.929698	9.9972	1204	1.65	155	2.75	T	98	0.82	2
9	2021-10-15T10:44:26	502.943889	9.9821	1204	1.65	156	2.59	T	98	0.82	3
9	2021-10-15T11:04:52	502.958081	9.9672	1204	1.65	152	2.54	T	98	0.82	4
10	2021-10-16T10:56:00	503.951960	9.7415	1204	1.65	130	0.85	T	92	0.89	1
10	2021-10-16T11:16:32	503.966216	9.7265	1204	1.66	145	0.85	T	92	0.89	2
10	2021-10-16T11:37:04	503.980473	9.7118	1204	1.68	141	0.85	T	90	0.89	3
10	2021-10-16T11:57:30	503.994665	9.6976	1204	1.70	134	0.88	T	90	0.89	4
11	2021-10-18T10:20:43	505.927524	9.2950	1204	1.65	137	3.05	T	77	0.98	1
11	2021-10-18T10:41:15	505.941780	9.2798	1204	1.65	136	3.07	T	77	0.98	2
11	2021-10-18T11:01:47	505.956036	9.2647	1204	1.66	142	3.17	T	77	0.98	3
11	2021-10-18T11:22:13	505.970227	9.2499	1204	1.67	143	3.15	T	77	0.98	4
12	2021-10-20T10:23:54	507.929789	8.8095	1204	1.65	145	5.63	T	66	-0.99	1
12	2021-10-20T10:44:20	507.943982	8.7943	1204	1.65	145	5.79	T	66	-0.99	2
12	2021-10-20T11:04:46	507.958173	8.7793	1204	1.66	142	5.82	T	66	-0.99	3
12	2021-10-20T11:25:12	507.972368	8.7646	1204	1.68	139	6.01	T	66	-0.99	4
13	2021-10-21T10:33:20	508.936373	8.5569	1204	1.65	148	3.10	T	61	-0.97	1
13	2021-10-21T10:53:46	508.950565	8.5418	1204	1.66	147	2.98	T	61	-0.97	2
13	2021-10-21T11:14:18	508.964820	8.5268	1204	1.68	144	2.88	T	61	-0.97	3
13	2021-10-21T11:34:44	508.979012	8.5123	1204	1.70	147	3.01	T	61	-0.97	4
14	2021-10-22T10:44:04	509.943857	8.3007	1204	1.66	111	2.15	T	58	-0.93	1
14	2021-10-22T11:04:36	509.958114	8.2856	1204	1.67	111	2.17	T	58	-0.93	2
14	2021-10-22T11:25:02	509.972306	8.2710	1204	1.69	110	2.26	T	58	-0.93	3

Table F.1. continued from previous page.

Epoch	UT Date	BJD	BERV ($km\,s^{-1}$)	Exp. time (sec)	Airmass	S/N at 1670 nm	H_2O rel. abs.	Moon on-sky	Moon (°)	Moon phase	Pol. seq. number
14	2021-10-22T11:45:28	509.986497	8.2567	1204	1.72	110	2.28	T	58	-0.93	4
15	2021-10-23T10:12:50	510.922184	8.0731	1204	1.65	149	3.08	T	56	-0.93	1
15	2021-10-23T10:33:16	510.936376	8.0579	1204	1.65	145	3.12	T	56	-0.87	2
15	2021-10-23T10:53:47	510.950632	8.0427	1204	1.66	143	3.27	T	56	-0.87	3
15	2021-10-23T11:14:14	510.964823	8.0279	1204	1.68	146	3.27	T	56	-0.87	4
16	2021-10-24T11:20:08	511.968953	7.7703	1204	1.69	120	1.76	T	56	-0.80	1
16	2021-10-24T11:40:34	511.983145	7.7560	1204	1.72	127	1.84	T	56	-0.80	2
16	2021-10-24T12:01:00	511.997337	7.7422	1204	1.76	118	1.84	T	56	-0.80	3
17	2021-10-26T09:50:42	513.906896	7.3218	1204	1.65	147	2.36	T	61	-0.72	1
17	2021-10-26T10:11:14	513.921151	7.3063	1204	1.65	147	2.33	T	61	-0.72	2
17	2021-10-26T10:31:40	513.935343	7.2910	1204	1.66	145	2.45	T	61	-0.63	3
17	2021-10-26T10:52:06	513.949535	7.2759	1204	1.67	139	2.57	T	61	-0.63	4
18	2021-11-13T06:36:44	531.772487	2.4459	1204	1.76	131	1.99	T	88	0.69	1
18	2021-11-13T06:57:10	531.786678	2.4312	1204	1.73	138	2.15	T	88	0.69	2
18	2021-11-13T07:17:42	531.800934	2.4160	1204	1.70	143	2.20	T	88	0.69	3
18	2021-11-13T07:38:08	531.815126	2.4005	1204	1.68	144	2.26	T	88	0.69	4
19	2021-11-17T09:58:59	535.912967	1.1234	1204	1.71	115	5.06	T	62	0.96	1
19	2021-11-17T10:19:31	535.927223	1.1089	1204	1.75	79	5.31	T	62	0.96	2
19	2021-11-17T10:40:03	535.941479	1.0948	1204	1.79	83	5.98	T	62	0.99	3
19	2021-11-17T11:00:29	535.955670	1.0815	1204	1.84	91	6.18	T	62	0.99	4
20	2021-11-20T08:16:08	538.841557	0.3204	1204	1.65	147	1.30	T	56	-0.99	1
20	2021-11-20T08:36:40	538.855808	0.3044	1204	1.65	147	1.29	T	56	-0.99	2
20	2021-11-20T08:57:12	538.870065	0.2886	1204	1.66	149	1.22	T	56	-0.99	3
20	2021-11-20T09:17:38	538.884257	0.2731	1204	1.68	148	1.19	T	56	-0.99	4
21	2021-11-21T08:28:22	539.850042	0.0164	1204	1.65	157	1.07	T	57	-0.96	1
21	2021-11-21T08:48:54	539.864298	0.0006	1204	1.66	157	1.08	T	57	-0.96	2
21	2021-11-21T09:09:25	539.878554	-0.0151	1204	1.67	155	1.10	T	57	-0.96	3
21	2021-11-21T09:29:52	539.892747	-0.0303	1204	1.69	152	1.15	T	57	-0.96	4
22	2021-12-09T07:21:22	557.803364	-5.2062	1204	1.65	119	2.49	T	97	0.32	1
22	2021-12-09T07:41:54	557.817620	-5.2219	1204	1.66	116	2.48	T	97	0.32	2
22	2021-12-09T08:02:26	557.831874	-5.2373	1204	1.68	117	2.51	T	97	0.32	3
22	2021-12-09T08:22:52	557.846067	-5.2524	1204	1.70	119	2.48	T	97	0.32	4
23	2021-12-11T06:42:23	559.776247	-5.7413	1204	1.65	118	2.95	T	82	0.53	1
23	2021-12-11T07:02:54	559.790503	-5.7572	1204	1.65	120	2.92	T	82	0.53	2
23	2021-12-11T07:23:26	559.804759	-5.7729	1204	1.65	128	2.90	T	82	0.53	3
23	2021-12-11T07:43:52	559.818950	-5.7884	1204	1.67	123	2.98	T	80	0.53	4
24	2021-12-12T06:41:13	560.775428	-6.0201	1204	1.65	139	2.53	T	74	0.63	1
24	2021-12-12T07:01:45	560.789685	-6.0359	1204	1.65	139	2.57	T	75	0.63	2
24	2021-12-12T07:22:17	560.803939	-6.0516	1204	1.66	140	2.69	T	75	0.63	3
24	2021-12-12T07:42:43	560.818130	-6.0670	1204	1.67	140	2.77	T	75	0.63	4
25	2021-12-13T07:08:52	561.794605	-6.3189	1204	1.65	113	3.42	T	69	0.72	1
25	2021-12-13T07:29:24	561.808859	-6.3345	1204	1.66	117	3.72	T	69	0.72	2
25	2021-12-13T07:49:55	561.823115	-6.3497	1204	1.68	125	4.17	T	69	0.72	3
25	2021-12-13T08:10:22	561.837306	-6.3646	1204	1.70	120	4.21	T	69	0.72	4
26	2021-12-14T06:15:31	562.757530	-6.5535	1204	1.65	152	3.18	T	64	0.81	1
26	2021-12-14T06:36:02	562.771786	-6.5693	1204	1.65	154	2.98	T	64	0.81	2
26	2021-12-14T06:56:29	562.785977	-6.5849	1204	1.65	154	2.88	T	64	0.81	3
26	2021-12-14T07:16:55	562.800168	-6.6005	1204	1.66	155	2.85	T	64	0.81	4
27	2021-12-15T06:25:47	563.764642	-6.8348	1204	1.65	123	0.67	T	60	0.88	1
27	2021-12-15T06:46:19	563.778898	-6.8506	1204	1.65	119	0.70	T	60	0.88	2
27	2021-12-15T07:06:50	563.793154	-6.8662	1204	1.65	114	0.71	T	60	0.88	3
27	2021-12-15T07:27:17	563.807345	-6.8815	1204	1.67	127	0.72	T	60	0.88	4
28	2021-12-16T07:14:59	564.798782	-7.1435	1204	1.66	140	1.26	T	57	0.93	1
28	2021-12-16T07:35:30	564.813036	-7.1587	1204	1.68	144	1.28	T	57	0.93	2
28	2021-12-16T07:56:02	564.827292	-7.1736	1204	1.70	135	1.34	T	57	0.93	3
28	2021-12-16T08:16:28	564.841483	-7.1880	1204	1.73	138	1.42	T	57	0.93	4
29	2021-12-18T06:47:02	566.779331	-7.6582	1204	1.65	150	3.30	T	56	0.99	1
29	2021-12-18T07:07:34	566.793582	-7.6736	1204	1.66	160	3.32	T	56	0.99	2
29	2021-12-18T07:28:06	566.807838	-7.6887	1204	1.68	157	3.44	T	56	0.99	3
29	2021-12-18T07:48:32	566.822028	-7.7035	1204	1.70	161	3.50	T	56	0.99	4
30	2022-01-06T06:29:30	585.766520	-12.2163	1204	1.70	137	2.39	T	92	0.17	1

Table F.1. continued from previous page.

Epoch	UT Date	BJD	BERV ($km\,s^{-1}$)	Exp. time (sec)	Airmass	S/N at 1670 nm	H_2O rel. abs.	Moon on-sky	Moon (°)	Moon phase	Pol. seq. number
30	2022-01-06T06:49:57	585.780715	-12.2299	1204	1.72	138	2.69	T	92	0.17	2
30	2022-01-06T07:10:28	585.794967	-12.2431	1204	1.76	107	2.66	T	92	0.17	3
30	2022-01-06T07:30:54	585.809157	-12.2556	1204	1.80	110	2.67	T	92	0.17	4
31	2022-01-08T06:41:25	587.774707	-12.6328	1204	1.72	148	0.96	T	77	0.36	1
31	2022-01-08T07:01:57	587.788963	-12.6458	1204	1.76	151	1.01	T	77	0.36	2
31	2022-01-08T07:22:28	587.803217	-12.6583	1204	1.80	151	1.06	T	77	0.36	3
31	2022-01-08T07:43:00	587.817472	-12.6702	1204	1.85	148	1.13	T	78	0.36	4
32	2022-01-10T06:10:19	589.753025	-13.0040	1204	1.69	152	2.61	T	66	0.56	1
32	2022-01-10T06:30:51	589.767280	-13.0175	1204	1.72	154	2.68	T	66	0.56	2
32	2022-01-10T06:51:22	589.781535	-13.0305	1204	1.75	153	2.69	T	65	0.56	3
32	2022-01-10T07:11:48	589.795727	-13.0429	1204	1.80	154	2.67	T	65	0.56	4
33†	2022-01-12T06:36:43	591.771269	-13.3958	1204	1.74	133	0.99	T	58	0.74	1
33†	2022-01-12T06:57:14	591.785525	-13.4083	1204	1.78	129	1.05	T	58	0.74	2
33†	2022-01-12T07:17:46	591.799780	-13.4202	1204	1.83	133	1.12	T	58	0.74	3
33†	2022-01-12T07:38:12	591.813970	-13.4314	1204	1.89	139	1.15	T	58	0.74	4
34	2022-01-13T05:02:35	592.705859	-13.5142	1204	1.65	159	1.20	T	56	0.82	1
34	2022-01-13T05:23:06	592.720111	-13.5284	1204	1.66	154	1.26	T	56	0.82	2
34	2022-01-13T05:43:38	592.734367	-13.5423	1204	1.68	157	1.33	T	56	0.82	3
34	2022-01-13T06:04:04	592.748557	-13.5559	1204	1.70	158	1.34	T	56	0.82	4
35	2022-01-15T06:31:35	594.767572	-13.9225	1204	1.75	146	2.28	T	58	0.94	1
35	2022-01-15T06:52:07	594.781827	-13.9346	1204	1.80	136	2.24	T	58	0.94	2
35	2022-01-15T07:12:33	594.796017	-13.9461	1204	1.85	152	2.27	T	58	0.94	3
35	2022-01-15T07:33:05	594.810273	-13.9569	1204	1.91	159	2.30	T	58	0.94	4
36	2022-01-18T05:51:37	597.739680	-14.3897	1204	1.71	151	1.27	T	71	-1.00	1
36	2022-01-18T06:12:09	597.753935	-14.4024	1204	1.74	151	1.30	T	71	-1.00	2
36	2022-01-18T06:32:35	597.768126	-14.4146	1204	1.78	152	1.35	T	71	-1.00	3
36	2022-01-18T06:53:01	597.782317	-14.4261	1204	1.83	152	1.40	T	71	-1.00	4
37	2022-01-19T06:18:59	598.758635	-14.5620	1204	1.76	145	1.30	T	77	-0.98	1
37	2022-01-19T06:39:31	598.772889	-14.5738	1204	1.80	149	1.37	T	77	-0.98	2
37	2022-01-19T07:00:03	598.787145	-14.5849	1204	1.86	153	1.42	T	77	-0.98	3
37	2022-01-19T07:20:29	598.801335	-14.5953	1204	1.92	153	1.45	T	77	-0.98	4
38	2022-01-20T05:59:54	599.745337	-14.7018	1204	1.73	152	2.81	F	84	-0.94	1
38	2022-01-20T06:20:26	599.759591	-14.7140	1204	1.77	149	3.02	F	84	-0.94	2
38	2022-01-20T06:40:58	599.773850	-14.7256	1204	1.82	152	3.20	T	84	-0.94	3
38	2022-01-20T07:01:24	599.788038	-14.7364	1204	1.87	151	3.39	T	84	-0.94	4
39	2022-01-21T05:56:31	600.742939	-14.8467	1204	1.73	144	3.24	F	91	-0.88	1
39	2022-01-21T06:16:58	600.757130	-14.8588	1204	1.77	142	3.33	F	91	-0.88	2
39	2022-01-21T06:37:24	600.771321	-14.8703	1204	1.82	147	3.49	F	91	-0.88	3
39	2022-01-21T06:57:50	600.785511	-14.8811	1204	1.87	146	3.59	F	91	-0.88	4
40	2022-01-22T05:55:23	601.742089	-14.9888	1204	1.74	119	1.64	F	98	-0.81	1
40	2022-01-22T06:15:54	601.756344	-15.0008	1204	1.78	123	1.77	F	98	-0.81	2
40	2022-01-22T06:36:26	601.770599	-15.0121	1204	1.82	118	1.85	F	98	-0.81	3
40	2022-01-22T06:56:52	601.784791	-15.0228	1204	1.88	104	1.92	F	98	-0.81	4
41	2022-01-23T06:03:58	602.748012	-15.1322	1204	1.76	151	2.34	F	105	-0.72	1
41	2022-01-23T06:24:30	602.762267	-15.1438	1204	1.80	146	2.28	F	105	-0.72	2
41	2022-01-23T06:45:02	602.776521	-15.1547	1204	1.86	144	2.25	F	105	-0.72	3
41	2022-01-23T07:05:28	602.790713	-15.1648	1204	1.92	147	2.33	F	105	-0.72	4
42	2022-01-24T06:19:05	603.758450	-15.2746	1204	1.80	157	2.52	F	112	-0.62	1
42	2022-01-24T06:39:37	603.772704	-15.2855	1204	1.85	156	2.70	F	111	-0.62	2
42	2022-01-24T07:00:08	603.786959	-15.2956	1204	1.92	156	2.90	F	111	-0.62	3
42	2022-01-24T07:20:34	603.801150	-15.3049	1204	1.99	155	3.20	F	111	-0.62	4
43	2022-01-25T06:29:43	604.765791	-15.4096	1204	1.84	124	2.11	F	116	-0.51	1
43	2022-01-25T06:50:15	604.780045	-15.4199	1204	1.90	124	2.18	F	115	-0.51	2
43	2022-01-25T07:10:47	604.794300	-15.4294	1204	1.97	129	2.23	F	117	-0.51	3
43	2022-01-25T07:31:13	604.808491	-15.4380	1204	2.05	124	2.32	F	117	-0.51	4
44†★	2022-01-26T06:37:52	605.774581	-15.5406	652	1.90	75	4.28	F	121	-0.40	1
45	2022-01-27T05:39:40	606.730932	-15.6273	1204	1.74	128	2.54	F	122	-0.29	1
45	2022-01-27T06:00:12	606.745188	-15.6388	1204	1.78	124	2.42	F	122	-0.29	2
45	2022-01-27T06:20:44	606.759443	-15.6497	1204	1.83	123	2.38	F	122	-0.29	3
45	2022-01-27T06:41:10	606.773634	-15.6599	1204	1.89	122	2.42	F	122	-0.29	4
46	2022-01-28T05:44:06	607.733950	-15.7455	1204	1.76	143	0.51	F	123	-0.19	1

Table F.1. continued from previous page.

Epoch	UT Date	BJD	BERV ($km\,s^{-1}$)	Exp. time (sec)	Airmass	S/N at 1670 nm	H_2O rel. abs.	Moon on-sky	Moon (°)	Moon phase	Pol. seq. number
46	2022-01-28T06:04:37	607.748206	-15.7567	1204	1.80	116	0.50	F	123	-0.19	2
46	2022-01-28T06:25:09	607.762461	-15.7673	1204	1.86	118	0.52	F	123	-0.19	3
46	2022-01-28T06:45:35	607.776651	-15.7771	1204	1.92	107	0.55	F	123	-0.19	4

Appendix G: RV and polarimetry data tables

Table G.1. SPIRou LBL RV observations of TOI-1695 obtained with APERO v6. The D^3V is the third derivative of LBL profiles with respect to radial velocity. It is a proxy for the BIS variations (see text for explanation).

BJD -2,459,000	v_r ($km\,s^{-1}$)	σ_{v_r} ($km\,s^{-1}$)	FWHM ($km\,s^{-1}$)	σ_{FWHM} ($km\,s^{-1}$)	D^3V $(km\,s^{-1})^{-3}$	σ_{D^3V} $(km\,s^{-1})^{-3}$
208.79493816	-59.9476	0.0066	5.527	0.014	-0.053	0.027
208.80919391	-59.9474	0.0064	5.526	0.014	-0.036	0.027
208.82344915	-59.9404	0.0063	5.524	0.014	-0.029	0.026
208.83770450	-59.9471	0.0064	5.529	0.014	-0.041	0.027
213.75864561	-59.9192	0.0060	5.533	0.013	-0.018	0.025
213.77290070	-59.9255	0.0061	5.512	0.013	-0.030	0.025
213.78715749	-59.9290	0.0060	5.532	0.013	-0.024	0.025
213.80141198	-59.9199	0.0063	5.533	0.013	-0.022	0.026
472.98091030	-59.9349	0.0059	5.485	0.013	-0.014	0.024
472.99516782	-59.9289	0.0057	5.486	0.012	-0.005	0.024
473.00936133	-59.9328	0.0057	5.478	0.012	0.007	0.024
473.02355075	-59.9301	0.0057	5.475	0.012	-0.007	0.024
476.88360128	-59.9372	0.0063	5.474	0.014	0.018	0.026
476.89779088	-59.9340	0.0061	5.462	0.013	-0.011	0.025
476.91204768	-59.9288	0.0062	5.456	0.013	-0.029	0.025
476.92623878	-59.9308	0.0062	5.456	0.013	-0.003	0.025
479.86476628	-59.9310	0.0058	5.457	0.013	-0.012	0.024
479.87902237	-59.9284	0.0056	5.453	0.012	-0.011	0.024
479.89321505	-59.9282	0.0057	5.457	0.012	-0.015	0.023
479.90740723	-59.9338	0.0057	5.465	0.012	-0.020	0.023
480.87194906	-59.9313	0.0061	5.475	0.013	-0.031	0.025
480.88620644	-59.9303	0.0061	5.465	0.013	-0.049	0.026
480.90039831	-59.9250	0.0060	5.470	0.013	-0.035	0.025
480.91458968	-59.9281	0.0060	5.477	0.013	-0.012	0.025
481.85700461	-59.9358	0.0059	5.457	0.013	-0.018	0.025
481.87119917	-59.9356	0.0058	5.443	0.013	-0.032	0.024
481.88538804	-59.9370	0.0058	5.425	0.012	-0.011	0.024
481.89958051	-59.9333	0.0058	5.433	0.012	-0.024	0.024
501.92949642	-59.9339	0.0060	5.478	0.013	-0.026	0.025
501.94375341	-59.9382	0.0059	5.485	0.013	-0.022	0.025
501.95800989	-59.9363	0.0058	5.487	0.013	-0.008	0.024
501.97220128	-59.9305	0.0058	5.480	0.013	0.003	0.024
502.91544136	-59.9373	0.0059	5.476	0.013	-0.039	0.025
502.92969804	-59.9416	0.0059	5.474	0.013	-0.009	0.024
502.94388941	-59.9353	0.0059	5.477	0.013	-0.042	0.025
502.95808148	-59.9427	0.0060	5.490	0.013	-0.006	0.025
503.95195991	-59.9548	0.0061	5.492	0.013	-0.020	0.025
503.96621637	-59.9445	0.0056	5.502	0.012	-0.029	0.023
503.98047314	-59.9413	0.0057	5.487	0.012	-0.013	0.023
503.99466510	-59.9429	0.0058	5.498	0.013	-0.015	0.024
505.92752409	-59.9379	0.0062	5.508	0.013	-0.029	0.026
505.94177953	-59.9400	0.0061	5.498	0.013	-0.025	0.025
505.95603647	-59.9418	0.0061	5.473	0.013	-0.027	0.025
505.97022731	-59.9358	0.0060	5.514	0.013	-0.007	0.025
507.92978917	-59.9286	0.0064	5.469	0.014	-0.026	0.027
507.94398159	-59.9208	0.0063	5.472	0.014	-0.019	0.026
507.95817331	-59.9222	0.0063	5.471	0.014	-0.022	0.026

Table G.1. continued from previous page

BJD -2,459,000	v_r (km s^{-1})	σ_{v_r} (km s^{-1})	FWHM (km s^{-1})	σ_{FWHM} (km s^{-1})	D^{3}V (km s^{-1})$^{-3}$	$\sigma_{\mathrm{D^3V}}$ (km s^{-1})$^{-3}$
507.97236802	-59.9235	0.0064	5.469	0.014	-0.017	0.026
508.93637316	-59.9311	0.0060	5.495	0.013	-0.017	0.025
508.95056467	-59.9371	0.0059	5.496	0.013	-0.016	0.025
508.96482027	-59.9373	0.0060	5.499	0.013	-0.022	0.025
508.97901207	-59.9280	0.0060	5.519	0.013	-0.013	0.025
509.94385745	-59.9250	0.0073	5.490	0.016	0.000	0.030
509.95811414	-59.9231	0.0072	5.489	0.015	-0.036	0.030
509.97230573	-59.9348	0.0072	5.496	0.016	-0.034	0.030
509.98649743	-59.9347	0.0072	5.526	0.016	-0.013	0.030
510.92218401	-59.9222	0.0062	5.490	0.014	-0.023	0.026
510.93637590	-59.9131	0.0062	5.518	0.014	-0.017	0.026
510.95063248	-59.9140	0.0063	5.500	0.014	-0.029	0.027
510.96482346	-59.9139	0.0061	5.487	0.014	-0.020	0.026
511.96895286	-59.9232	0.0067	5.531	0.014	-0.021	0.027
511.98314483	-59.9198	0.0064	5.518	0.013	-0.027	0.026
511.99733669	-59.9306	0.0067	5.518	0.014	-0.016	0.027
513.90689610	-59.9232	0.0057	5.491	0.012	-0.026	0.024
513.92115105	-59.9252	0.0056	5.496	0.012	-0.015	0.023
513.93534260	-59.9270	0.0057	5.502	0.012	-0.039	0.024
513.94953504	-59.9273	0.0059	5.495	0.013	-0.040	0.025
531.77248693	-59.9328	0.0069	5.526	0.015	-0.034	0.029
531.78667804	-59.9338	0.0063	5.496	0.014	-0.031	0.026
531.80093355	-59.9376	0.0061	5.510	0.013	-0.062	0.025
531.81512557	-59.9268	0.0061	5.518	0.013	-0.048	0.025
535.91296729	-59.9410	0.0077	5.490	0.016	-0.036	0.031
535.92722294	-59.9531	0.0112	5.538	0.024	-0.070	0.045
535.94147939	-59.9292	0.0106	5.537	0.023	-0.101	0.044
535.95567034	-59.9257	0.0097	5.554	0.021	-0.073	0.040
538.84155732	-59.9325	0.0056	5.485	0.012	-0.038	0.024
538.85580844	-59.9317	0.0057	5.501	0.012	-0.050	0.024
538.87006465	-59.9355	0.0057	5.501	0.012	-0.036	0.024
538.88425656	-59.9297	0.0056	5.496	0.012	-0.027	0.024
539.85004231	-59.9332	0.0056	5.489	0.012	-0.040	0.024
539.86429831	-59.9276	0.0056	5.476	0.012	-0.042	0.023
539.87855411	-59.9345	0.0056	5.501	0.012	-0.048	0.023
539.89274681	-59.9326	0.0057	5.473	0.012	-0.045	0.023
557.80336435	-59.9221	0.0072	5.554	0.016	-0.026	0.030
557.81761950	-59.9161	0.0074	5.555	0.016	-0.035	0.030
557.83187445	-59.9272	0.0073	5.553	0.016	-0.028	0.030
557.84606670	-59.9196	0.0071	5.541	0.015	-0.040	0.029
559.77624676	-59.9350	0.0077	5.541	0.016	-0.060	0.031
559.79050318	-59.9408	0.0074	5.561	0.016	-0.036	0.030
559.80475871	-59.9346	0.0068	5.564	0.015	-0.054	0.028
559.81894984	-59.9353	0.0069	5.564	0.015	-0.039	0.029
560.77542835	-59.9428	0.0063	5.539	0.014	-0.033	0.026
560.78968516	-59.9381	0.0062	5.520	0.013	-0.013	0.025
560.80393897	-59.9466	0.0061	5.533	0.013	-0.032	0.025
560.81812999	-59.9446	0.0060	5.516	0.013	-0.034	0.025
561.79460490	-59.9219	0.0078	5.555	0.016	-0.032	0.031
561.80885940	-59.9272	0.0075	5.585	0.016	-0.040	0.031
561.82311469	-59.9326	0.0073	5.569	0.016	-0.039	0.030
561.83730619	-59.9371	0.0074	5.555	0.016	-0.028	0.031
562.75753023	-59.9328	0.0060	5.527	0.013	-0.027	0.025
562.77178552	-59.9345	0.0058	5.518	0.013	-0.030	0.025
562.78597711	-59.9320	0.0058	5.512	0.013	-0.041	0.024
562.80016759	-59.9267	0.0058	5.511	0.013	-0.027	0.024
563.76464181	-59.9453	0.0066	5.546	0.014	-0.005	0.026
563.77889829	-59.9400	0.0067	5.536	0.014	-0.050	0.027
563.79315376	-59.9405	0.0067	5.531	0.014	-0.023	0.027
563.80734474	-59.9301	0.0061	5.527	0.013	-0.049	0.025
564.79878234	-59.9410	0.0061	5.565	0.013	-0.035	0.025

Table G.1. continued from previous page

BJD -2,459,000	v_r (km s^{-1})	σ_{v_r} (km s^{-1})	FWHM (km s^{-1})	$\sigma_{\rm FWHM}$ (km s^{-1})	D^{3}V (km s^{-1})$^{-3}$	$\sigma_{\rm D^3V}$ (km s^{-1})$^{-3}$
564.81303560	-59.9329	0.0060	5.521	0.013	-0.018	0.024
564.82729206	-59.9388	0.0061	5.534	0.013	-0.035	0.025
564.84148262	-59.9299	0.0061	5.542	0.013	-0.049	0.025
566.77933148	-59.9446	0.0063	5.522	0.014	-0.055	0.026
566.79358211	-59.9428	0.0061	5.519	0.013	-0.032	0.025
566.80783755	-59.9503	0.0062	5.536	0.013	-0.024	0.026
566.82202828	-59.9385	0.0061	5.540	0.013	-0.046	0.025
585.76652048	-59.9380	0.0064	5.551	0.014	-0.013	0.027
585.78071470	-59.9383	0.0064	5.539	0.014	-0.010	0.026
585.79496722	-59.9291	0.0079	5.575	0.017	-0.037	0.033
585.80915704	-59.9367	0.0075	5.578	0.016	-0.035	0.032
587.77470698	-59.9397	0.0056	5.512	0.012	-0.011	0.023
587.78896268	-59.9365	0.0056	5.478	0.012	-0.007	0.023
587.80321708	-59.9375	0.0056	5.510	0.012	-0.012	0.023
587.81747208	-59.9402	0.0055	5.499	0.012	-0.000	0.023
589.75302522	-59.9403	0.0062	5.508	0.013	-0.007	0.026
589.76728010	-59.9335	0.0062	5.490	0.013	-0.039	0.025
589.78153548	-59.9306	0.0062	5.519	0.013	-0.026	0.025
589.79572667	-59.9318	0.0061	5.489	0.013	-0.007	0.025
592.70585888	-59.9231	0.0061	5.495	0.013	-0.009	0.025
592.72011124	-59.9234	0.0061	5.505	0.013	-0.022	0.025
592.73436680	-59.9242	0.0060	5.519	0.013	-0.035	0.025
592.74855726	-59.9241	0.0060	5.522	0.013	-0.021	0.024
594.76757159	-59.9434	0.0066	5.536	0.014	-0.018	0.027
594.78182683	-59.9326	0.0069	5.530	0.015	-0.035	0.028
594.79601747	-59.9382	0.0063	5.512	0.014	-0.014	0.026
594.81027260	-59.9363	0.0060	5.521	0.013	-0.031	0.025
597.73968050	-59.9398	0.0057	5.508	0.012	-0.001	0.023
597.75393471	-59.9394	0.0057	5.503	0.012	-0.001	0.023
597.76812613	-59.9385	0.0056	5.519	0.012	-0.018	0.023
597.78231695	-59.9362	0.0056	5.506	0.012	-0.019	0.023
598.75863479	-59.9294	0.0062	5.511	0.013	-0.033	0.025
598.77288920	-59.9320	0.0060	5.521	0.013	-0.019	0.025
598.78714471	-59.9302	0.0059	5.520	0.013	-0.016	0.025
598.80133531	-59.9404	0.0060	5.517	0.013	-0.026	0.025
599.74533714	-59.9339	0.0064	5.475	0.014	-0.027	0.026
599.75959124	-59.9358	0.0061	5.505	0.013	0.003	0.025
599.77384994	-59.9391	0.0060	5.506	0.013	-0.006	0.025
599.78803765	-59.9324	0.0060	5.508	0.013	-0.036	0.024
600.74293878	-59.9394	0.0063	5.538	0.014	-0.025	0.026
600.75712977	-59.9377	0.0061	5.523	0.013	-0.039	0.025
600.77132087	-59.9407	0.0061	5.536	0.013	-0.016	0.025
600.78551106	-59.9409	0.0062	5.526	0.013	-0.015	0.026
601.74208946	-59.9335	0.0076	5.549	0.016	-0.040	0.030
601.75634424	-59.9354	0.0071	5.541	0.015	-0.027	0.029
601.77059913	-59.9397	0.0073	5.561	0.015	-0.008	0.029
601.78479052	-59.9290	0.0083	5.598	0.018	-0.004	0.034
602.74801173	-59.9299	0.0060	5.518	0.013	-0.015	0.025
602.76226731	-59.9290	0.0060	5.533	0.013	-0.007	0.025
602.77652129	-59.9253	0.0060	5.495	0.013	-0.017	0.025
602.79071298	-59.9300	0.0058	5.500	0.013	0.000	0.024
603.75844953	-59.9340	0.0063	5.482	0.014	-0.018	0.026
603.77270410	-59.9382	0.0061	5.485	0.013	-0.026	0.025
603.78695928	-59.9429	0.0061	5.484	0.013	-0.002	0.025
603.80115015	-59.9489	0.0061	5.510	0.013	-0.025	0.025
604.76579074	-59.9210	0.0071	5.562	0.015	-0.022	0.029
604.78004541	-59.9281	0.0069	5.557	0.015	-0.029	0.028
604.79430017	-59.9295	0.0064	5.539	0.014	-0.025	0.027
604.80849134	-59.9340	0.0067	5.559	0.015	-0.037	0.028
606.73093229	-59.9328	0.0070	5.566	0.015	-0.007	0.029
606.74518775	-59.9433	0.0071	5.549	0.015	-0.025	0.029

Table G.1. continued from previous page

BJD -2,459,000	v_r (km s^{-1})	σ_{v_r} (km s^{-1})	FWHM (km s^{-1})	$\sigma_{\rm FWHM}$ (km s^{-1})	D^{3}V (km s^{-1})$^{-3}$	$\sigma_{\rm D^3V}$ (km s^{-1})$^{-3}$
606.75944270	-59.9392	0.0071	5.557	0.015	-0.032	0.029
606.77363376	-59.9428	0.0069	5.539	0.015	-0.026	0.029
607.73395032	-59.9287	0.0062	5.514	0.013	-0.039	0.025
607.74820557	-59.9363	0.0074	5.545	0.016	-0.034	0.030
607.76246093	-59.9318	0.0070	5.533	0.015	-0.021	0.028
607.77665138	-59.9256	0.0078	5.564	0.016	-0.024	0.030

Table G.2. SPIRou LBL RV observations of TOI-1695 obtained with APERO v7.

BJD -2,459,000	v_r (km s^{-1})	σ_{v_r} (km s^{-1})	FWHM (km s^{-1})	$\sigma_{\rm FWHM}$ (km s^{-1})	D^{3}V (km s^{-1})$^{-3}$	$\sigma_{\rm D^3V}$ (km s^{-1})$^{-3}$
208.79493816	-59.4531	0.0084	5.8675	0.018	-0.002	0.033
208.80919391	-59.4712	0.0064	5.7880	0.014	-0.011	0.027
208.82344915	-59.4654	0.0063	5.7882	0.014	-0.004	0.027
208.83770450	-59.4662	0.0065	5.7769	0.014	-0.016	0.028
213.75864561	-59.4454	0.0062	5.7935	0.013	0.001	0.026
213.77290070	-59.4544	0.0061	5.7817	0.013	0.010	0.026
213.78715749	-59.4551	0.0061	5.7930	0.013	-0.005	0.026
213.80141198	-59.4483	0.0063	5.7954	0.014	0.004	0.027
472.98091030	-59.4657	0.0057	5.7911	0.012	-0.007	0.024
472.99516782	-59.4577	0.0056	5.7730	0.012	0.006	0.024
473.00936133	-59.4672	0.0056	5.7632	0.012	0.018	0.024
473.02355075	-59.4615	0.0056	5.7823	0.012	-0.004	0.023
476.88360128	-59.4672	0.0062	5.7740	0.014	0.018	0.027
476.89779088	-59.4646	0.0061	5.7706	0.013	-0.005	0.026
476.91204768	-59.4671	0.0060	5.7695	0.013	-0.006	0.026
476.92623878	-59.4618	0.0060	5.7687	0.013	-0.007	0.026
479.86476628	-59.4563	0.0057	5.7578	0.012	-0.008	0.024
479.87902237	-59.4511	0.0057	5.7536	0.012	-0.009	0.024
479.89321505	-59.4542	0.0056	5.7515	0.012	-0.005	0.024
479.90740723	-59.4604	0.0056	5.7654	0.012	-0.003	0.024
480.87194906	-59.4620	0.0058	5.7839	0.013	-0.009	0.025
480.88620644	-59.4627	0.0058	5.7716	0.013	-0.029	0.025
480.90039831	-59.4544	0.0058	5.7647	0.013	-0.028	0.025
480.91458968	-59.4555	0.0059	5.7744	0.013	0.008	0.025
481.85700461	-59.4616	0.0058	5.7705	0.013	-0.012	0.025
481.87119917	-59.4676	0.0057	5.7683	0.012	-0.016	0.024
481.88538804	-59.4636	0.0057	5.7367	0.012	-0.010	0.024
481.89958051	-59.4597	0.0056	5.7474	0.012	-0.020	0.024
501.92949642	-59.4617	0.0059	5.7822	0.013	-0.018	0.025
501.94375341	-59.4641	0.0059	5.7733	0.013	-0.015	0.025
501.95800989	-59.4665	0.0059	5.7847	0.013	0.007	0.025
501.97220128	-59.4564	0.0059	5.7808	0.013	0.003	0.025
502.91544136	-59.4598	0.0061	5.7711	0.013	-0.018	0.026
502.92969804	-59.4637	0.0060	5.7617	0.013	0.003	0.026
502.94388941	-59.4621	0.0060	5.7726	0.013	-0.012	0.026
502.95808148	-59.4689	0.0060	5.7901	0.013	0.005	0.026
503.95195991	-59.4779	0.0060	5.7833	0.013	-0.009	0.025
503.96621637	-59.4718	0.0055	5.7844	0.012	-0.015	0.023
503.98047314	-59.4717	0.0055	5.7966	0.012	-0.013	0.023
503.99466510	-59.4689	0.0057	5.7794	0.012	-0.003	0.024
505.92752409	-59.4635	0.0060	5.7910	0.013	-0.026	0.025
505.94177953	-59.4672	0.0061	5.7887	0.013	-0.022	0.026
505.95603647	-59.4689	0.0059	5.7718	0.013	-0.009	0.025
505.97022731	-59.4604	0.0058	5.7931	0.013	-0.000	0.025
507.92978917	-59.4545	0.0062	5.7577	0.014	-0.007	0.027
507.94398159	-59.4490	0.0061	5.7651	0.013	-0.006	0.026
507.95817331	-59.4504	0.0061	5.7491	0.013	-0.013	0.026

Table G.2. continued from previous page

BJD -2,459,000	v_r (km s^{-1})	σ_{v_r} (km s^{-1})	FWHM (km s^{-1})	$\sigma_{\rm FWHM}$ (km s^{-1})	D^{3}V (km s^{-1})$^{-3}$	$\sigma_{\rm D^3V}$ (km s^{-1})$^{-3}$
507.97236802	-59.4451	0.0062	5.7546	0.013	-0.013	0.026
508.93637316	-59.4568	0.0059	5.7890	0.013	-0.008	0.025
508.95056467	-59.4624	0.0059	5.7848	0.013	-0.015	0.025
508.96482027	-59.4631	0.0060	5.7795	0.013	-0.021	0.025
508.97901207	-59.4581	0.0059	5.7913	0.013	-0.021	0.025
509.94385745	-59.4552	0.0070	5.7879	0.015	-0.009	0.030
509.95811414	-59.4496	0.0070	5.7608	0.015	-0.027	0.030
509.97230573	-59.4670	0.0070	5.7817	0.015	-0.019	0.030
509.98649743	-59.4686	0.0070	5.8111	0.015	-0.013	0.030
510.92218401	-59.4565	0.0058	5.7855	0.013	-0.022	0.025
510.93637590	-59.4478	0.0059	5.7871	0.013	-0.015	0.025
510.95063248	-59.4534	0.0060	5.7824	0.013	-0.028	0.025
510.96482346	-59.4489	0.0059	5.7599	0.013	-0.021	0.025
511.96895286	-59.4491	0.0065	5.8208	0.014	-0.014	0.028
511.98314483	-59.4547	0.0062	5.8100	0.013	-0.028	0.026
511.99733669	-59.4650	0.0066	5.8064	0.014	-0.018	0.028
513.90689610	-59.4572	0.0056	5.7917	0.012	-0.034	0.024
513.92115105	-59.4618	0.0055	5.7801	0.012	-0.025	0.023
513.93534260	-59.4638	0.0056	5.7952	0.012	-0.033	0.024
513.94953504	-59.4601	0.0057	5.7967	0.012	-0.033	0.024
531.77248693	-59.4610	0.0069	5.8188	0.015	-0.000	0.029
531.78667804	-59.4636	0.0065	5.7800	0.014	-0.015	0.027
531.80093355	-59.4657	0.0061	5.7979	0.013	-0.027	0.025
531.81512557	-59.4576	0.0061	5.7894	0.013	-0.010	0.025
535.91296729	-59.4633	0.0073	5.7752	0.016	-0.006	0.031
535.92722294	-59.4559	0.0103	5.8492	0.023	-0.040	0.044
535.94147939	-59.4496	0.0099	5.8508	0.022	-0.044	0.043
535.95567034	-59.4333	0.0090	5.8318	0.020	-0.048	0.039
538.84155732	-59.4670	0.0056	5.7769	0.012	-0.027	0.024
538.85580844	-59.4628	0.0057	5.7716	0.012	-0.033	0.024
538.87006465	-59.4751	0.0057	5.7695	0.012	-0.034	0.024
538.88425656	-59.4688	0.0057	5.7742	0.012	-0.017	0.024
539.85004231	-59.4689	0.0056	5.7647	0.012	-0.030	0.023
539.86429831	-59.4651	0.0055	5.7558	0.012	-0.000	0.023
539.87855411	-59.4692	0.0055	5.7668	0.012	-0.021	0.023
539.89274681	-59.4692	0.0056	5.7679	0.012	-0.020	0.024
557.80336435	-59.4724	0.0070	5.8099	0.015	0.011	0.030
557.81761950	-59.4710	0.0071	5.8210	0.015	0.026	0.030
557.83187445	-59.4715	0.0070	5.8075	0.015	0.021	0.030
557.84606670	-59.4715	0.0069	5.8090	0.015	0.018	0.029
559.77624676	-59.4681	0.0073	5.7912	0.016	-0.006	0.031
559.79050318	-59.4750	0.0071	5.8125	0.015	0.005	0.030
559.80475871	-59.4731	0.0066	5.8147	0.014	-0.006	0.028
559.81894984	-59.4692	0.0069	5.8231	0.015	-0.004	0.029
560.77542835	-59.4681	0.0063	5.7951	0.014	-0.010	0.027
560.78968516	-59.4721	0.0060	5.7848	0.013	0.007	0.025
560.80393897	-59.4731	0.0059	5.8008	0.013	-0.007	0.025
560.81812999	-59.4709	0.0058	5.7846	0.013	-0.013	0.025
561.79460490	-59.4529	0.0075	5.8266	0.017	-0.008	0.032
561.80885940	-59.4580	0.0074	5.8299	0.016	-0.009	0.032
561.82311469	-59.4722	0.0072	5.8262	0.016	-0.014	0.031
561.83730619	-59.4668	0.0071	5.8188	0.016	-0.000	0.030
562.75753023	-59.4580	0.0060	5.7945	0.013	-0.023	0.025
562.77178552	-59.4651	0.0059	5.8029	0.013	-0.007	0.025
562.78597711	-59.4584	0.0058	5.7839	0.013	-0.031	0.025
562.80016759	-59.4530	0.0057	5.7840	0.013	-0.010	0.024
563.76464181	-59.4655	0.0063	5.8150	0.014	0.009	0.026
563.77889829	-59.4657	0.0066	5.7974	0.014	-0.016	0.027
563.79315376	-59.4632	0.0066	5.7884	0.014	-0.009	0.027
563.80734474	-59.4589	0.0061	5.7839	0.013	-0.027	0.025
564.79878234	-59.4646	0.0060	5.8243	0.013	-0.004	0.025

Table G.2. continued from previous page

BJD -2,459,000	v_r (km s^{-1})	σ_{v_r} (km s^{-1})	FWHM (km s^{-1})	σ_{FWHM} (km s^{-1})	D^{3}V (km s^{-1})$^{-3}$	$\sigma_{\mathrm{D^3V}}$ (km s^{-1})$^{-3}$
564.81303560	-59.4591	0.0059	5.8107	0.013	0.004	0.025
564.82729206	-59.4647	0.0062	5.8055	0.013	-0.011	0.026
564.84148262	-59.4614	0.0060	5.8159	0.013	-0.006	0.025
566.77933148	-59.4741	0.0067	5.7850	0.015	-0.022	0.029
566.79358211	-59.4721	0.0065	5.7605	0.014	-0.004	0.028
566.80783755	-59.4771	0.0067	5.7811	0.015	0.007	0.029
566.82202828	-59.4656	0.0065	5.7960	0.014	-0.033	0.028
585.76652048	-59.4594	0.0068	5.8175	0.015	-0.001	0.029
585.78071470	-59.4601	0.0067	5.7761	0.014	-0.006	0.028
585.79496722	-59.4660	0.0080	5.8302	0.017	0.018	0.034
585.80915704	-59.4590	0.0077	5.8197	0.017	-0.008	0.033
587.77470698	-59.4634	0.0057	5.7748	0.012	0.005	0.024
587.78896268	-59.4610	0.0056	5.7658	0.012	-0.001	0.023
587.80321708	-59.4624	0.0056	5.7784	0.012	-0.000	0.023
587.81747208	-59.4612	0.0055	5.7682	0.012	0.013	0.023
589.75302522	-59.4619	0.0061	5.7736	0.013	-0.014	0.026
589.76728010	-59.4594	0.0060	5.7631	0.013	-0.023	0.026
589.78153548	-59.4571	0.0059	5.7856	0.013	-0.014	0.025
589.79572667	-59.4578	0.0060	5.7794	0.013	0.005	0.025
591.77126900	-59.4521	0.0060	5.8048	0.013	-0.036	0.025
591.78552487	-59.4560	0.0060	5.7901	0.013	-0.032	0.025
591.79978033	-59.4588	0.0060	5.7753	0.013	-0.023	0.025
591.81397029	-59.4540	0.0057	5.7920	0.012	-0.010	0.024
592.70585888	-59.4500	0.0063	5.7629	0.014	-0.020	0.026
592.72011124	-59.4573	0.0062	5.7706	0.013	-0.017	0.026
592.73436680	-59.4582	0.0061	5.7728	0.013	-0.030	0.026
592.74855726	-59.4583	0.0063	5.7868	0.014	-0.001	0.026
594.76757159	-59.4715	0.0069	5.7864	0.015	-0.002	0.029
594.78182683	-59.4658	0.0071	5.7823	0.015	-0.019	0.030
594.79601747	-59.4743	0.0065	5.7616	0.014	0.007	0.028
594.81027260	-59.4677	0.0063	5.7637	0.014	0.003	0.027
597.73968050	-59.4661	0.0056	5.7792	0.012	-0.004	0.024
597.75393471	-59.4646	0.0056	5.7788	0.012	-0.007	0.023
597.76812613	-59.4661	0.0054	5.7850	0.012	-0.009	0.023
597.78231695	-59.4655	0.0054	5.7863	0.012	-0.011	0.023
598.75863479	-59.4584	0.0063	5.7973	0.014	-0.017	0.026
598.77288920	-59.4642	0.0062	5.8018	0.013	-0.015	0.026
598.78714471	-59.4606	0.0062	5.7775	0.013	-0.002	0.026
598.80133531	-59.4692	0.0060	5.7917	0.013	-0.017	0.025
599.74533714	-59.4562	0.0061	5.7671	0.013	-0.015	0.026
599.75959124	-59.4670	0.0059	5.7894	0.013	0.009	0.025
599.77384994	-59.4649	0.0058	5.7783	0.013	0.000	0.025
599.78803765	-59.4605	0.0058	5.7853	0.013	-0.025	0.025
600.74293878	-59.4719	0.0064	5.8115	0.014	-0.029	0.027
600.75712977	-59.4654	0.0063	5.7874	0.014	-0.045	0.027
600.77132087	-59.4672	0.0062	5.7938	0.014	-0.013	0.026
600.78551106	-59.4695	0.0062	5.7853	0.014	-0.011	0.026
601.74208946	-59.4553	0.0070	5.8273	0.015	-0.025	0.029
601.75634424	-59.4568	0.0068	5.8079	0.015	-0.027	0.029
601.77059913	-59.4661	0.0070	5.8272	0.015	-0.015	0.029
601.78479052	-59.4454	0.0078	5.8485	0.017	-0.004	0.033
602.74801173	-59.4522	0.0060	5.7973	0.013	-0.012	0.025
602.76226731	-59.4602	0.0058	5.8083	0.013	-0.001	0.024
602.77652129	-59.4490	0.0058	5.7821	0.013	-0.000	0.024
602.79071298	-59.4566	0.0057	5.7914	0.012	-0.006	0.024
603.75844953	-59.4634	0.0061	5.7663	0.013	-0.009	0.026
603.77270410	-59.4690	0.0059	5.7794	0.013	-0.016	0.025
603.78695928	-59.4704	0.0059	5.7685	0.013	0.001	0.025
603.80115015	-59.4784	0.0059	5.7862	0.013	-0.002	0.025
604.76579074	-59.4525	0.0069	5.8172	0.015	-0.018	0.029
604.78004541	-59.4554	0.0067	5.8201	0.015	-0.038	0.029

Table G.2. continued from previous page

BJD -2,459,000	v_r (km s^{-1})	σ_{v_r} (km s^{-1})	FWHM (km s^{-1})	$\sigma_{\rm FWHM}$ (km s^{-1})	D^{3}V (km s^{-1})$^{-3}$	$\sigma_{\rm D^3V}$ (km s^{-1})$^{-3}$
604.79430017	-59.4523	0.0065	5.8048	0.014	-0.021	0.028
604.80849134	-59.4634	0.0067	5.8235	0.015	-0.025	0.028
606.73093229	-59.4486	0.0072	5.8098	0.016	-0.018	0.031
606.74518775	-59.4544	0.0072	5.7984	0.016	-0.045	0.031
606.75944270	-59.4588	0.0073	5.8186	0.016	-0.035	0.031
606.77363376	-59.4635	0.0072	5.8029	0.016	-0.031	0.031

Table G.3. B_ℓ and null polarization N observations of TOI-1695.

BJD -2,459,000	B_ℓ (G)	σ_B (G)	N	σ_N	EqW (Å)
473.0016398	-4.12	4.99	5.00	4.87	1.651
476.9045374	-3.21	3.17	1.46	3.36	1.954
479.8851662	1.73	3.12	1.11	3.26	1.944
480.8918336	-1.24	3.43	-2.74	3.55	1.930
481.8775293	-2.05	3.12	-6.80	3.40	1.942
501.9502817	-1.85	3.24	-1.71	3.30	1.813
502.9355799	1.16	3.08	0.02	3.17	1.898
503.9727203	-1.88	3.70	3.94	3.71	1.802
505.9486172	3.73	3.60	6.75	3.73	1.792
507.9496392	0.35	3.70	-6.78	3.82	1.830
508.9567142	6.69	3.39	-0.73	3.51	1.915
509.9643374	-2.14	5.07	-4.97	5.20	1.793
510.9424300	1.40	3.29	-5.95	3.33	1.955
513.9267436	3.88	3.30	-1.46	3.37	1.918
531.7939318	3.00	3.49	2.10	3.66	1.930
535.9308136	-2.69	8.20	-2.33	7.68	1.738
538.8621726	0.39	3.11	2.17	3.19	1.961
539.8701053	-2.49	2.92	-0.01	3.14	1.946
557.8238866	0.52	5.16	-3.23	5.19	1.752
559.7975022	-0.53	4.85	-4.68	4.96	1.785
560.7960801	-3.17	3.54	-1.15	3.60	1.877
561.8158711	4.28	4.91	-5.31	4.91	1.792
562.7782783	0.94	3.15	-2.67	3.18	1.932
563.7854884	3.39	4.40	-4.50	4.45	1.897
564.8188796	0.44	3.96	-2.45	4.08	1.890
566.8006265	0.62	3.32	-1.53	3.40	1.890
585.7837539	0.41	4.69	0.73	6.50	1.776
589.7735483	-3.04	3.03	-1.98	3.38	1.975
591.7921350	1.51	3.68	1.54	3.72	1.947
592.7261387	-3.25	2.99	2.83	3.11	1.967
594.7893179	-7.56	3.65	-9.50	4.00	1.613
597.7601225	-2.01	4.08	-0.30	4.21	1.586
599.7656805	0.53	2.87	-4.19	2.98	1.895
600.7635277	3.07	4.20	-1.51	4.24	1.655
601.7610720	6.95	5.31	5.46	5.43	1.739
602.7681757	1.18	3.65	-6.27	3.77	1.712
603.7787482	1.05	3.64	-1.39	3.82	1.704
606.7510680	6.67	5.46	4.70	5.63	1.662